

Chandra Archival Sample of Intracluster Entropy Profiles

KENNETH. W. CAVAGNOLO¹, MEGAN DONAHUE, G. MARK VOIT, AND MING SUN
 Department of Physics and Astronomy, BPS Building, Michigan State University, East Lansing, MI 48824
 Draft version July 13, 2008

ABSTRACT

We present radial entropy profiles of the intracluster medium (ICM) for a collection of 233 clusters taken from the *Chandra* X-ray Observatory’s Data Archive. ICM entropy is of great interest because it dictates ICM global properties and records the thermal history of a cluster. Entropy is therefore a useful quantity for studying the effects of feedback on the cluster environment and investigating the breakdown of cluster self-similarity. We find that most ICM entropy profiles are well-fit by a model which is a power-law at large radii and approaches a constant value at small radii: $K(r) = K_0 + K_{100}(r/100 \text{ kpc})^\alpha$, where K_0 quantifies the typical excess of core entropy above the best fitting power-law found at larger radii. We also show that the K_0 distributions of both the full archival sample and the primary *HIFLUGCS* sample of Reiprich (2001) are bimodal with a distinct gap beginning at $K_0 \approx 30 \text{ keV cm}^2$ and population peaks at $K_0 \sim 15 \text{ keV cm}^2$ and $K_0 \sim 150 \text{ keV cm}^2$. The effect of PSF smearing and angular resolution on best-fit K_0 values are investigated using mock *Chandra* observations and degraded entropy profiles, respectively. We find that neither of these effects is sufficient to explain the entropy profile flattening we measure. The influence of profile curvature and number of radial bins on best-fit K_0 is also considered, and we find no indication K_0 is significantly impacted by either. All code, data, and results associated with *ACCEPT* are publicly available via the project web site.

Subject headings: conduction – cooling flows – galaxies: active – galaxies: clusters: general – X-rays: galaxies: clusters – galaxies: evolution

1. INTRODUCTION

The general process of galaxy cluster formation through hierarchical merging is well understood, but many details, such as the impact of feedback sources on the cluster environment and radiative cooling in the cluster core, are not. The nature of feedback operating within clusters is of great interest because of the implications for ~~better understanding massive galaxy formation and using~~ mass-observable scaling relations in cluster cosmological studies. Early models of structure formation which included only gravitation predicted self-similarity among the galaxy cluster population. ~~That is to say,~~ the physical properties of galaxy clusters, such as temperature and luminosity, ~~sealed~~ with cluster redshift and mass (Kaiser 1986; Evrard & Henry 1991; Navarro et al. 1995, 1997; Evrard et al. 1996; Evrard 1997; Teyssier et al. 1997; Eke et al. 1998; Bryan & Norman 1998). However, numerous observational studies have shown clusters do not follow the predicted simple, ~~low-scatter~~ mass-observable scaling relations (Edge & Stewart 1991; Allen & Fabian 1998; Markevitch 1998; Arnaud & Evrard 1999; Horner et al. 1999; Nevalainen et al. 2000; Finoguenov et al. 2001). To reconcile observation with theory, it was realized non-gravitational effects, such as heating and radiative cooling in cluster cores, could not be neglected if models were to accurately replicate the process of cluster formation, *e.g.* Loewenstein (2000) and Borgani et al. (2002).

As a consequence of radiative cooling, best-fit total cluster temperature decreases while total cluster luminosity increases. In addition, feedback sources such as active galactic nuclei (AGN) and supernovae can drive cluster cores (where most of the cluster flux originates) away from hydrostatic equilibrium. Thus, at a given mass scale, radiative cooling and feedback conspire to create dispersion in otherwise tight mass-observable correlations like mass-luminosity and mass-

temperature. While considerable progress has been made both observationally and theoretically in the areas of understanding, quantifying, and reducing scatter in cluster scaling-relations (Buote & Tsai 1996; Jeltama et al. 2005; Kravtsov et al. 2006; Nagai et al. 2007; Ventimiglia et al. 2008), it is still important to understand how, taken as a whole, non-gravitational processes affect cluster formation and evolution.

An ~~appurtenant~~ issue to the departure of clusters from self-similarity is that of cooling flows in cluster cores. The core cooling time in 50%-66% of clusters is much shorter than both the Hubble time and cluster age (Stewart et al. 1984; Edge et al. 1992; White et al. 1997; Peres et al. 1998; Bauer et al. 2005). For such clusters (and without compensatory heating), radiative cooling will result in the formation a cooling flow (see Fabian 1994, for a review)). Early estimates put the mass deposition rates from cooling flows in the range of $100 - 1000 M_\odot \text{ yr}^{-1}$, (Jones & Forman 1984, *e.g.*). However, cooling flow mass deposition rates inferred from soft X-ray spectroscopy were found to be significantly less than predicted, with the ICM never reaching temperatures lower than $T_{\text{virial}}/3$ (Tamura et al. 2001; Peterson et al. 2001, 2003; Kaastra et al. 2004). Irrespective of system mass, the massive torrents of cool gas turned out to be more like cooling trickles.

In addition to the lack of soft X-ray line emission from cooling flows, prior methodical searches for the end products of cooling flows (*i.e.* molecular gas and emission line nebulae) revealed far less mass is locked-up in by-products than expected (Heckman et al. 1989; McNamara et al. 1990; O’Dea et al. 1994; Voit & Donahue 1995). The disconnects between observation and theory have been termed “the cooling flow problem” and raise the question, “Where has all the cool gas gone?” The substantial amount of observational evidence suggests some combination of energetic feedback sources ~~have~~ heated the ICM to selectively remove gas with a short cooling time and establish quasi-stable thermal balance of the ICM.

¹ cavagnolo@pa.msu.edu

Both the breakdown of self-similarity and the cooling flow problem point toward the need for better understanding cluster feedback and radiative cooling. Recent revisions to models of how clusters form and evolve by including feedback sources has led to better agreement between observation and theory (Bower et al. 2006; Croton et al. 2006; Saro et al. 2006). The current paradigm regarding the cluster feedback process holds that AGN are the primary heat delivery mechanism and that an AGN outburst deposits the requisite energy into the ICM to retard, and in some cases quench, cooling (see McNamara & Nulsen 2007, for a review). How the feedback loop functions is still the topic of much debate, but that AGN are interacting with the hot atmospheres of clusters is no longer in doubt as evidenced by the prevalence of bubbles in clusters Birzan et al. (2004). **One robust observable which has proven useful in studying the effect of non-gravitational processes is ICM entropy.**

Taken individually, ICM temperature and density do not fully reveal a cluster's thermal history ~~because these quantities are most influenced by the underlying dark matter potential~~. Gas temperature reflects the depth of the potential well, while density reflects the capacity of the well to compress the gas. However, at constant pressure the density of a gas is determined by its specific entropy. Rewriting the expression for the ~~adiabat~~, $K \equiv P\rho^{-5/3}$, in terms of temperature and electron density, one can define a new quantity, $K = kT_X n_e^{-2/3}$, where kT_X is temperature and n_e is electron gas density. This new quantity, K , captures the thermal history of the gas because only ~~heating and cooling~~ can change K . This quantity is commonly referred to as entropy, but in actuality the classic thermodynamic entropy is $s = \ln K^{3/2} + \text{constant}$.

One important property of gas entropy is that a gas cloud is convectively stable when $dK/dr \geq 0$. Thus, gravitational potential wells are giant entropy sorting devices: low entropy gas sinks to the bottom of the potential well, while high entropy gas buoyantly rises to a radius of equal entropy. If cluster evolution proceeded under the influence of gravitation only, then the radial entropy distribution of clusters would exhibit power-law behavior for $r > 0.1r_{200}$ with a constant, low entropy core at small radii (Voit et al. 2002). Thus, large-scale departures of the radial entropy distribution from a power-law can be used to measure the ~~effect~~ of processes such as AGN heating and radiative cooling. Several studies have found that the radial ICM entropy distribution in some clusters flattens ~~outside~~ $0.1r_{500}$ (David et al. 1996; Ponman et al. 1999; Lloyd-Davies et al. 2000; Ponman et al. 2003; Piffaretti et al. 2005; Donahue et al. 2005, 2006; Morandi & Ettori 2007). These previous studies utilized smaller, focused samples and we have undertaken a much larger study utilizing the *Chandra* Data Archive.

In this paper we present the data and results from a *Chandra* archival project in which we studied the ICM entropy distribution for 233 galaxy clusters. We have named this project the “Archive of *Chandra* Cluster Entropy Profile Tables,” or *ACCEPT* for short. In contrast to the sample of nine classic cooling flow clusters studied in Donahue et al. (2006, hereafter D06), *ACCEPT* covers a broader range of luminosities, temperatures, and morphologies, focusing on more than just cooling flow clusters. One of our primary objectives for this project was to provide the research community with an additional resource to study cluster evolution and confront current models with a ~~broad range~~ of entropy profiles.

We have found that the departure of entropy profiles from a

~~self-similar power-law is not limited to cooling flow clusters, but~~ is a feature of most clusters, and given high enough angular resolution, possibly all clusters. We also find that the core entropy distribution of both the full *ACCEPT* collection and the Highest X-Ray Flux Galaxy Cluster Sample (*HIFLUGCS*, Reiprich 2001; Reiprich & Böhringer 2002) are bimodal. In a separate letter (Cavagnolo et al. 2008a), we present results that show indicators of feedback - ~~namely~~ radio sources assumed to be associated with AGN and $H\alpha$ emission assumed to be the result of thermal instability formation - are strongly correlated with core entropy.

A key aspect of this project is the dissemination of all data and results to the public. We have created a searchable, interactive web site² which hosts all of our results. The *ACCEPT* web site is ~~being~~ continually updated as new *Chandra* cluster and group observations are archived and analyzed. The web site provides all data tables, plots, spectra, reduced *Chandra* data products (~~forthcoming~~), reduction scripts, and more. Given the large number of clusters in our sample, figures, fits, and tables showing/listing results for individual clusters have been omitted and are available at the *ACCEPT* web site.

The structure of this paper is as follows: In §2 we outline initial sample selection criteria and information about the *Chandra* observations selected under these criteria. Data reduction is discussed in §3. Spectral extraction and analysis are discussed in §3.1, while our method for deriving deprojected electron density profiles is outlined in §3.2. A few possible sources of systematics are discussed in §4. Results and discussion are presented in §5. A brief summary is given in §6. For this work we have assumed a flat Λ CDM Universe with cosmogony $\Omega_M = 0.3$, $\Omega_\Lambda = 0.7$, and $H_0 = 70 \text{ km s}^{-1} \text{ Mpc}^{-1}$. All quoted uncertainties are 90% confidence (1.6σ).

2. DATA COLLECTION

Our sample was initially collected from observations publicly available in the *Chandra* Data Archive (CDA) as of June 2006. We first assembled a list of targets from multiple flux-limited surveys: the *ROSAT* Brightest Cluster Sample (Ebeling et al. 1998), RBCS Extended Sample (Ebeling et al. 2000), *ROSAT* Brightest 55 Sample (Edge et al. 1990; Peres et al. 1998), *Einstein* Extended Medium Sensitivity Survey (Gioia et al. 1990), North Ecliptic Pole Survey (Henry et al. 2006), *ROSAT* Deep Cluster Survey (Rosati et al. 1995), *ROSAT* Serendipitous Survey (Vikhlinin et al. 1998), Massive Cluster Survey (Ebeling et al. 2001), and *REFLEX* Survey (Böhringer et al. 2004). After the first round of data analysis concluded, we continued to expand our collection by adding new archival data listed under the CDA Science Categories “clusters of galaxies” or “active galaxies”. As of submission, we have inspected all CDA clusters of galaxies observations and analyzed 510 of those observations (14.16 Msec). The Coma and Fornax clusters have been intentionally left out of our sample because they are very well studied nearby clusters which require a more intensive analysis than we undertook in this project.

The available data for some clusters limited our ability to derive an entropy profile. Calculation of entropy ~~requires~~ measurement of the radial gas temperature and density structures (discussed further in §3). To infer a temperature which is reasonably well constrained ($\Delta kT_X \approx \pm 1.0 \text{ keV}$) we imposed a minimum requirement of three temperature bins containing 2500 counts each. After applying this constraint, the

² <http://www.pa.msu.edu/astro/MC2/accept>

final sample presented in here has 310 observations of 233 clusters with a total exposure time of 9.66 Msec. The sample covers the temperatures range $kT_X \sim 1 - 20$ keV, a bolometric luminosity range of $L_{bol} \sim 10^{42-46}$ ergs s⁻¹, and redshifts of $z \sim 0.05 - 0.89$. Table 1 lists the general properties for each cluster in *ACCEPT*.

In section 5.4 we cull the *HIFLUGCS* primary sample (Reiprich 2001; Reiprich & Böhringer 2002) from our full archival collection. The groups M49, NGC 507, NGC 4636, NGC 5044, NGC 5813, and NGC 5846 are part of the *HIFLUGCS* primary sample but were not members of our initial archival sample. In order to take full advantage of the *HIFLUGCS* primary sample, we analyzed observations of these 6 groups. Note, however, that none of these 6 groups are included in the general discussion of *ACCEPT*.

We were unable to analyze some clusters for this study because of complications other than not meeting our minimum analysis requirements for analysis. These clusters were: 2PIGG J0311.8-2655, 3C 129, A168, A514, A753, A1367, A2634, A2670, A2877, A3074, A3128, A3627, AS0463, APMCC 0421, MACS J2243.3-0935, MS J1621.5+2640, RX J1109.7+2145, RX J1206.6+2811, RX J1423.8+2404, SDSS J198.070267-00.984433, Triangulum Australis, and Zw5247.

We also report $H\alpha$ observations taken by M. Donahue while a Carnegie Fellow. These observations were not utilized in this paper but are used in Cavagnolo et al. (2008a). The new $[NII]/H\alpha$ ratios and $H\alpha$ fluxes are listed in Table 3. The upper-limits listed in Table 3 are 3σ significance. The observations were taken with either the 5 m Hale Telescope at the Palomar Observatory, USA, or the DuPont 2.5 m telescope at the Las Campanas Observatory, Chile. All observations were made with a 2'' slit centered on the BCG using two position angles: one along the semi-major axis and one along the semi-minor axis of the galaxy. The overlap area was 10 pixels². The red light (555-798 nm) setup on the Hale Double Spectrograph used a 316 lines/mm grating with a dispersion of 0.31 nm/pixel and an effective resolution of 0.7-0.8 nm. The DuPont Modular Spectrograph setup included a 1200 lines/mm grating with a dispersion of 0.12 nm/pixel and an effective resolution of 0.3 nm. The statistical and calibration uncertainties for the observations are both $\sim 10\%$. The statistical uncertainty arises primarily from variability of the spectral continuum and hence imperfect background subtraction.

3. DATA ANALYSIS

Measuring radial ICM entropy first requires measurement of radial ICM temperature and density. The radial temperature structure of each cluster was measured by fitting a single-temperature thermal model to spectra extracted from concentric annuli centered on the cluster X-ray “center”. As discussed in Cavagnolo et al. (2008b), the ICM X-ray peak of the point-source cleaned, exposure-corrected cluster image was used as the cluster center, unless the iteratively determined X-ray centroid was more than 70 kpc away from the X-ray peak, in which case the centroid was used as the radial analysis zero-point. To derive the gas density profile, we first deprojected an exposure-corrected, background-subtracted, point source clean surface brightness profile extracted in the 0.7-2.0 keV energy range to attain a volume emission density. This emission density, along with spectroscopic information (count rate and normalization in each annulus), was then used to calculate gas density. The resulting entropy profiles were then fit with two models: a simple model which has only a radial power-

law component, and a model which is the sum of a constant core entropy term, K_0 and the radial power-law component.

In this paper we cover the basics of deriving gas entropy from X-ray observables, and direct interested readers to D06 for in-depth discussion of our data reprocessing and reduction, and Cavagnolo et al. (2008b) for details regarding determination of each cluster’s “center” and how the X-ray background was handled. The only difference between the analysis presented in this paper and that of D06 and Cavagnolo et al. (2008b), is that we have used newer versions of CIAO and the CALDB (CIAO 3.4.1 and CALDB 3.4.0).

3.1. Temperature Profiles

One of the two components needed to derive a gas entropy profile is the temperature as a function of radius. We therefore constructed radial temperature profiles for each cluster in our collection. To reliably constrain a temperature, and allow for the detection of temperature structure beyond isothermality, we required each temperature profile to have a minimum of three annuli containing 2500 counts each. The annuli for each cluster were generated by first extracting a background-subtracted cumulative counts profile using 1 pixel width annular bins originating from the cluster center and extending to a radius bounded by the detector edge, or $0.5R_{180}$, whichever was smaller. Profiles were truncated at $0.5R_{180}$ as we are most interested in the radial entropy behavior of cluster core regions ($r \lesssim 100$ kpc) and $0.5R_{180}$ is the approximate radius where temperature profiles turnover (Vikhlinin et al. 2005). Additionally, analysis of diffuse gas temperature structure at large radii, which spectroscopically is dominated by background, requires a time consuming, observation-specific analysis of the X-ray background (see Sun et al. 2008, for an excellent detailed discussion on this point).

Cumulative counts profiles were divided into annuli containing at least 2500 counts. For well resolved clusters, the number of counts per annulus was increased to reduce the resulting uncertainty of kT_X and, for simplicity, to keep the number of annuli less than 50. The method we use to derive entropy profiles is most sensitive to the surface brightness radial bin size and not the resolution or uncertainties of the temperature profile. Thus, the loss of resolution in the temperature profile from increasing the number of counts per bin, and thereby reducing the number of annuli, has an insignificant effect on the final entropy profiles and best-fit entropy models.

Background analysis was performed using the blank-sky datasets provided in the CALDB. Backgrounds were reprocessed and reprojected to match each observation. Off-axis chips were used to normalize for variations of the hard-particle background by comparing blank-sky and observation 9.5-12 keV count rates. Soft residuals were also created and fitted for each observation to account for the spatially-varying soft Galactic background. This component was added as an additional, fixed background component during spectral fitting. Errors associated with the soft background are estimated and added in quadrature to the final error.

For each radial annular region, source and background spectra were extracted from the target cluster and corresponding normalized blank-sky dataset. Following standard CIAO techniques³ we created weighted response files (WARF) and redistribution matrices (WRMF) for each cluster using a flux-weighted map (WMAP) across the entire extraction region.

³ <http://cxc.harvard.edu/ciao/guides/esa.html>

These files quantify the effective area, quantum efficiency, and imperfect resolution of the *Chandra* instrumentation as a function of chip position. Each spectrum was binned to contain a minimum of 25 counts per energy bin.

Spectra were fitted with XSPEC 11.3.2ag (Arnaud 1996) using an absorbed, single-temperature MEKAL model (Mewe et al. 1985, 1986) over the energy range 0.7–7.0 keV. Neutral hydrogen column densities, N_H , were taken from Dickey & Lockman (1990). A comparison between the N_H values of Dickey & Lockman (1990) and the higher-resolution LAB Survey (Kalberla et al. 2005) revealed that the two surveys agree to within $\pm 20\%$ for 80% of the clusters in our sample. For the other 20% of the sample, using the LAB value, or allowing N_H to be free, did not result in best-fit temperatures or metallicities which differ significantly from fits using the Dickey & Lockman (1990) values.

The potentially free parameters of the absorbed thermal model are N_H , X-ray temperature, metal abundance normalized to Solar (Anders & Grevesse 1989, elemental ratios taken from), and a normalization proportional to the integrated emission measure within the extraction region,

$$\eta = \frac{10^{-14}}{4\pi D_A^2 (1+z)^2} \int n_e n_p dV, \quad (1)$$

where D_A is the angular diameter distance, z is cluster redshift, n_e and n_p are the electron and proton densities respectively, and V is the volume of the emission region. In all fits the metal abundance in each annulus was a free parameter and N_H was fixed to the Galactic value. No systematic error is added during fitting and thus all quoted errors are statistical only. The statistic used during fitting was χ^2 (XSPEC statistics package CHI). All uncertainties were calculated using 90% confidence.

For some clusters, more than one observation was available in the archive. We utilized the combined exposure time by first extracting independent spectra, WARFs, WRMFs, normalized background spectra, and soft residuals for each observation. These independent spectra were then read into XSPEC simultaneously and fit with the same spectral model which had all parameters, except normalization, tied among the spectra.

As in D06, we find spectral deprojection does not result in significant differences between best-fit temperatures inferred for projected or deprojected quantities. Thus, for this work, we quote projected temperatures only. Deprojection of temperature should result in slightly lower temperatures in the central bins of only the clusters with the steepest temperature gradients. For these clusters, the end result would be a negligible lowering of the entropy for the central-most bins. We stress that spectral deprojection does not significantly change the shape of the entropy profiles nor the best-fit K_0 values.

3.2. Deprojected Electron Density Profiles

For predominantly free-free emission, emissivity strongly depends on density and only weakly on temperature, $\epsilon \propto \rho^2 T^{1/2}$. Therefore the measured flux in a narrow temperature range is an excellent measure of ICM density. To reconstruct the relevant gas density as a function of physical radius we deprojected the cluster emission from high-resolution surface brightness profiles and converted to electron density using normalizations and count rates taken from the spectral analysis.

We extracted surface brightness profiles from the 0.7–2.0 keV energy range using concentric annular bins of size $5''$

originating from the cluster center. Each surface brightness profile was corrected with an observation specific, normalized radial exposure profile to remove the effects of vignetting and exposure time fluctuations. Following the recommendation in the CIAO guide for analyzing extended sources, exposure maps were created using the monoenergetic value associated with the observed count rate peak. The more sophisticated method of creating exposure maps using spectral weights calculated for an incident spectrum with the temperature and metallicity of the observed cluster was also tested. For the narrow energy band we consider, the chip response is relatively flat and we find no significant differences between the two methods. For all clusters the monoenergetic value used in creating exposure maps was between 0.8–1.7 keV.

The 0.7–2.0 keV spectroscopic count rate and spectral normalization were interpolated from the radial temperature profile grid to match the surface brightness radial grid. Utilizing the deprojection technique of Kriss et al. (1983), the interpolated spectral parameters were used to convert observed surface brightness to deprojected electron density. Radial electron density written in terms of relevant quantities is,

$$n_e(r) = \sqrt{\frac{4\pi [D_A(1+z)]^2 C(r) \eta(r)}{10^{-14} f(r) r_{ion}}} \quad (2)$$

where r_{ion} is an ionization ratio ($n_e = 1.2n_p$), $C(r)$ is the radial emission density derived from eqn. A1 in Kriss et al. (1983), η is the interpolated spectral normalization from eqn. 1, D_A is the angular diameter distance, z is cluster redshift, and $f(r)$ is the interpolated spectroscopic count rate. Cosmic dimming of source surface brightness is accounted for by the $D_A^2(1+z)^2$ term. This method of deprojection takes into account temperature and metallicity fluctuations which affect observed gas emissivity. Errors for the gas density profile were estimated using 5000 Monte Carlo simulations of the original surface brightness profile. The Kriss et al. (1983) deprojection technique assumes spherical symmetry, but it was shown in D06 such an assumption has little effect on final entropy profiles.

3.3. β -model Fits

Noisy surface brightness profiles, or profiles with irregularities such as inversions or extended flat cores, result in unstable, unphysical quantities when using the “onion” deprojection technique. For cases where deprojection of the raw data was problematic, we resorted to fitting the surface brightness profile with a β -model (Cavaliere & Fusco-Femiano 1978). It is well known that the β -model is ~~only an approximation for an isothermal gas distribution and~~ does not precisely represent all the features of the ICM (Ettori 2000; Loken et al. 2002; Hallman et al. 2007). However, for the profiles which required a fit, the β -model was a suitable approximation, and the model’s use was only a means for creating a smooth function which was easily deprojected. The single ($N = 1$) and double ($N = 2$) β -models were used in fitting,

$$S_x = \sum_{i=1}^N S_i \left[1 + \left(\frac{r}{r_{c,i}} \right)^2 \right]^{-3\beta_i + \frac{1}{2}}. \quad (3)$$

The models were fitted using Craig Markwardt’s robust non-linear least squares minimization IDL routines⁴. The data input to the fitting routines were weighted using the inverse square of the observational errors. Using this weighting

⁴ <http://cow.physics.wisc.edu/~craigm/idl/>

scheme resulted in residuals which were near unity for, on average, the inner 80% of the radial range considered. Accuracy of errors output from the fitting routine were checked against a bootstrap Monte Carlo analysis of 1000 surface brightness realizations. Both the single- and double- β models were fit to each profile and using the F-test functionality of *SHERPA*⁵ we determined if the addition of extra model components was justified given the degrees of freedom and χ^2 values of each fit. If the significance was less than 0.05, the extra components were justified and the double- β model was used.

A best-fit β -model was used in place of the data when deriving electron density for the clusters listed in Table 2. These clusters are also flagged in Table 1 with the note letter ‘a’. The best-fit β -models and background-subtracted, exposure-corrected surface brightness profiles are shown in Figure 1. See Appendix A for notes discussing individual clusters. The disagreement between the best-fit β -model and the surface brightness in the central regions for some clusters is also discussed in Appendix A. In short, the discrepancy arises from the presence of compact X-ray sources, a topic which is addressed in §3.5. All clusters requiring a β -model fit have $K_0 > 95 \text{ keV cm}^2$ and the mean best-fit parameters are listed in Table 4.

3.4. Entropy Profiles

Radial entropy profiles were calculated using the widely adopted formulation $K(r) = kT_x(r)n_e(r)^{-2/3}$. To create the radial entropy profiles, the temperature and density profiles must be on the same radial grid. This was accomplished by interpolating the temperature profile across the higher-resolution radial grid of the deprojected electron density profile. In general, because the density profile have higher radial resolution, the central bin of the temperature profile spans several bins of the density profile. Since we are most interested in the behavior of the entropy profiles in the central regions, how the interpolation was performed in this part of the profiles was important. Thus, temperature interpolation over the region of the density profile where a single central temperature bin encompasses several density profile bins was applied in two ways: (1) as a linear gradient consistent with the slope of the temperature profile at radii larger than the central T_X bin ($\Delta T_{\text{center}} \neq 0$), and (2) as a constant ($\Delta T_{\text{center}} = 0$). Shown in Figure 2 is the ratio of best-fit core entropy, K_0 , using the above two methods. The five points lying below the line of equality are clusters which are best-fit by a power-law or have K_0 statistically consistent with zero. It is worth noting that both schemes yield statistically consistent values for K_0 except for the clusters marked by red points which have a ratio significantly different from unity.

The clusters which significantly differ from one all have steep temperature gradients with the maximum and minimum radial temperatures differing by a factor of 1.3-5.0. Extrapolation of a steep temperature gradient as $r \rightarrow 0$ results in very low central temperatures (typically $T_X \leq T_{\text{virial}}/3$) which are inconsistent with observations, most notably Peterson et al. (2003). Most important however, is that the flattening of entropy we observe in the cores of our sample (discussed in §5.1) is *not* a result of the method chosen for interpolating the temperature profile. For this paper we therefore focus on the results derived assuming a constant temperature across the central-most bins.

Uncertainty in $K(r)$ arising from using a single-component temperature model for each annulus during spectral analysis contributes negligibly to our final fits and is discussed in detail in the Appendix of D06. Briefly summarizing D06: we have primarily measured the entropy of the lowest entropy gas because it is the most luminous gas. For the best-fit entropy values to be significantly changed, the volume filling fraction of a higher-entropy component must be non-trivial ($> 50\%$). As discussed in D06, our results are robust to the presence of multiple, low luminosity gas phases and mostly insensitive to X-ray surface brightness decrements, such as X-ray cavities and bubbles, although in extreme cases their influence on an entropy profile can be detected (for an example, see the cluster A2052).

Each entropy profile was fit with two models: a simple model which is a power-law at large radii and approaches a constant value at small radii (eqn. 4), and a model which is a power-law only (eqn. 5):

$$K(r) = K_0 + K_{100} \left(\frac{r}{100 \text{ kpc}} \right)^\alpha \quad (4)$$

$$K(r) = K_{100} \left(\frac{r}{100 \text{ kpc}} \right)^\alpha \quad (5)$$

In these models, K_0 is what we call core entropy, K_{100} is a normalization for entropy at 100 kpc, and α is the power-law index. Note, however, that K_0 does not necessarily represent the minimum core entropy or the entropy at $r = 0$. Nor does K_0 capture the gas entropy which would be measured immediately around an AGN or in a BCG X-ray corona. Instead, K_0 represents the typical excess of core entropy above the best fitting power-law at larger radii. Fits were truncated at a maximum radius (determined by eye) to avoid the influence of noisy bins at large radii which result from instability of our deprojection method. A listing of all the best-fit parameters for each cluster are published at the *ACCEPT* web site. The mean best-fit parameters for the full *ACCEPT* sample are given in Table 4. Also given in Table 4 are the mean best-fit parameters for clusters below and above $K_0 = 50 \text{ keV cm}^2$. We show in §5.2 that the cut at $K_0 = 50 \text{ keV cm}^2$ is not completely arbitrary as it approximately demarcates the division between two distinct populations in the K_0 distribution.

Some clusters have a surface brightness profile which is comparable to a double β -model. Our models for the behavior of $K(r)$ are intentionally simplistic and are not intended to fully describe all the features of $K(r)$. Thus, for the small number of clusters with discernible double- β behavior, fitting of the entropy profiles was restricted to the innermost of the two β -like features. These clusters have been flagged in Table 1 with the note letter ‘b’. The best-fit power-law index is typically much steeper for these clusters, but the outer regions, which we do not discuss here, have power-law indices which are typical of the rest of the sample, *i.e.* $\alpha \sim 1.2$.

3.5. Exclusion of Central Sources

For many clusters in our sample the ICM X-ray peak, ICM X-ray centroid, BCG optical emission, and BCG infrared emission are coincident or well within 70 kpc of one another. This made identification of the cluster center robust and trivial. However, in some clusters, there is an X-ray point source or compact X-ray source ($r \lesssim 5 \text{ kpc}$) found very near ($r < 10 \text{ kpc}$) the cluster center and always associated with a BCG. The 37 clusters discussed in this section are flagged in Table 1 with the note letter ‘d’ for AGN and ‘e’ for compact but resolved

⁵ <http://cxc.harvard.edu/ciao3.4/ahelp/fptest.html>

sources. The mean best-fit parameters for these clusters are given in Table 4 under the sample name ‘CSE’. These clusters cover the redshift range $z = 0.0044 - 0.4641$ with mean $z = 0.1196 \pm 0.1234$, and temperature range $kT_X = 1 - 12$ keV with mean $kT_X = 4.43 \pm 2.53$ keV. For some clusters – such as 3C 295, A2052, A426, Cygnus A, Hydra A, or M87 – the source is an AGN and there was no question the source must be removed.

However, determining how to handle the compact X-ray sources was not so straightforward. These compact sources are larger than the PSF, fainter than an AGN, but typically have significantly higher surface brightness than the surrounding ICM such that the compact source’s extent was distinguishable from the ICM. These sources are most prominent, and thus the most troublesome, in non-cool core clusters (*i.e.* clusters which are approximately isothermal). They are troublesome because the compact source is typically much cooler and denser than the surrounding ICM and hence has an entropy much lower than the ambient ICM. We suspect most of these compact sources are X-ray coronae associated with the BCG (Sun et al. 2007).

Without removing the compact sources, we derived radial entropy profiles and found, for all cases, that $K(r)$ abruptly changes at the outer edge of the compact source. Including the compact sources results in the central cluster region(s) appearing overdense, and at a given temperature the region will have a much lower entropy than if the source were excluded. Such a discontinuity in $K(r)$ results in our simple models of $K(r)$ not being a good description of the profiles. Aside from producing poor fits, a significantly lower entropy influences the value of best-fit parameters because the shape of $K(r)$ is drastically changed. Obviously, two solutions are available: exclude or keep the compact sources during analysis. Deciding what to do with these sources depends upon what cluster properties we are specifically interested in quantifying.

The compact X-ray sources discussed in this section are not representative of the cluster’s core entropy; these sources are representative of the entropy within and immediately surrounding peculiar BCGs. Our focus for the *ACCEPT* project was to quantify the entropy structure of the cluster core region, not to determine the minimum entropy of cluster cores or to quantify the entropy of peculiar core objects such as BCG coronae. Thus, we ~~concluded~~ to exclude these compact sources during our analysis. For a few extraordinary sources, it was simpler to ignore the central bin of the surface brightness profile during analysis because of imperfect exclusion of a compact source’s extended emission. These clusters have been flagged in Table 1 with the note letter ‘f’.

It is worth noting that when any source is excluded from the data, the empty pixels where the source once was were not included in the calculation of the surface brightness (counts and pixels are both excluded). Thus, the decrease in surface brightness of a bin where a source has been removed is not a result of the count to area ratio being artificially reduced.

4. SYSTEMATICS

Our models for $K(r)$ were designed so that the best-fit K_0 values are a good measure of the entropy profile flattening at small radii. This flattening could potentially be altered through the effects of systematics such as PSF smearing and surface brightness profile angular resolution. To quantify the extent to which our K_0 values are being affected by these systematics, we have analyzed mock *Chandra* obser-

vations created using the ray-tracing program MARX⁶, and also by analyzing degraded entropy profiles generated from artificially redshifting well-resolved clusters. In the analysis below we show that the lack of $K_0 \lesssim 10$ keV cm² at $z \gtrsim 0.1$ is attributable to resolution effects, but that deviation of an entropy profile from a power-law, even if only in the centralmost bin, cannot be accounted for by PSF effects.

4.1. PSF Effects

To assess the effect of PSF smearing on our entropy profiles, we have updated the analysis presented in §4.1 of D06 to use MARX simulations. In the D06 analysis, we assumed the density and temperature structure of the cluster core obeyed power-laws with $n_e \propto r^{-1}$ and $T_X \propto r^{1/3}$. This results in a power-law entropy profile with $K \propto r$. Further assuming the main emission mechanism is thermal bremsstrahlung, *i.e.* $\epsilon_X \propto T_X^{1/2}$, yields a surface brightness profile which has the form $S_X \propto r^{-5/6}$. A source image consistent with these parameters was created in IDL and then input to MARX to create the mock *Chandra* observations.

The MARX simulations were performed using the spectrum of a 4.0 keV, 0.3Z_⊙ abundance MEKAL model. We have tested using input spectra with $kT_X = 2 - 10$ keV with varying abundances and find the effect of temperature and metallicity on the distribution of photons in MARX to be insignificant for our discussion here. We have neglected the X-ray background in this analysis as it is overwhelmed by cluster emission in the core and is only important at large radii. Observations for both ACIS-S and ACIS-I instruments were simulated using an exposure time of 40 ksec. A surface brightness profile was then extracted from the mock observations using the same 5'' bins used on the real data.

For 5'' bins, we find the difference between the central bins of the input surface brightness and the output MARX observations to be less than the statistical uncertainty. One should expect this result, as the on-axis *Chandra* PSF is $\lesssim 1''$ and the surface brightness bins we have used on the data are five times this size. What is most interesting and important though, is that our analysis using MARX suggests any deviation of the surface brightness – and consequently the entropy profile – from a power-law, even if only in the central bin, is real and cannot be attributed to PSF effects. Even for the most poorly resolved clusters, the deviation away from a power-law we observe in ~~so many~~ of our entropy profiles is not an artifact of the data analysis or deprojection technique.

4.2. Angular Resolution Effects

Another possible limitation on evaluating K_0 is the effect of using fixed angular size bins for extracting surface brightness profiles. This choice may introduce a redshift-dependence into the best-fit K_0 values because as redshift increases, a fixed angular size encompasses a larger physical volume and the value of K_0 may increase if the bin includes a broad range of gas entropy. Shown in Figure 3 is a plot of the best-fit K_0 values for our entire sample versus redshift. At low redshift ($z < 0.02$), there are a few objects with $K_0 < 10$ keV cm² and only one at higher redshift (A1991 – $K_0 = 1.53 \pm 0.32$, $z = 0.0587$ – which is a very peculiar cluster (Sharma et al. 2004)). This raises the question: can the lack of clusters with $K_0 \lesssim 10$ keV cm² at $z > 0.02$ be completely explained by resolution effects?

⁶ <http://space.mit.edu/CXC/MARX/>

To answer this question we tested the ~~effect~~ redshift has on ~~measuring~~ K_0 by selecting all clusters with $K_0 \leq 10 \text{ keV cm}^2$ and $z \leq 0.1$ and degrading their surface brightness profiles to mimic the effect of increasing the cluster redshift. Our test is best illustrated using an example: consider a cluster at $z = 0.1$. For this cluster, $5'' \approx 9 \text{ kpc}$. Were the cluster at $z = 0.2$, $5''$ would equal $\approx 16 \text{ kpc}$. To mimic moving this example cluster from $z = 0.1 \rightarrow 0.2$, we can extract a new surface brightness profile using a bin size of 16 kpc instead of $5''$. This will result in a new surface brightness profile which has the angular resolution for a cluster at a higher redshift.

We used the preceding procedure to degrade the profiles of our subsample. New surface brightness bin sizes were calculated for each cluster over an evenly distributed grid of redshifts in the range $z = 0.1 - 0.4$ using step sizes of 0.02 . The temperature profiles for each cluster were also degraded by starting at the innermost temperature profile annulus and moving outward pairing-up neighboring annuli. New spectra were extracted for these enlarged regions and analyzed following the same procedure detailed in §3.1.

The ensemble of artificially redshifted clusters were analyzed using the procedure outlined in §3.4. The notable effects on the entropy profiles arising from lower angular resolution are: (1) less information about profile shape, and (2) increased entropy of the centralmost bins. Obviously, as redshift increases, the number of radial bins decreases. Fewer radial bins translates into ~~less detail~~ of an entropy profile's curvature, *e.g.* the profiles become less "curvy." On its own this effect should lead to lower best-fit K_0 values, but, while profile curvature is reduced, the entropy of the central-most bins is increasing because the bins encompass a broader range of entropy. From $z = 0.1 - 0.3$ this last effect dominates, resulting in an increase of $(K'_0 - K_0)/K_0 = 2.72 \pm 1.84$ where K_0 is the original best-fit value and K'_0 is the best-fit value of the degraded profiles. However, at $z > 0.3$, the loss of radial resolution dominates and the degraded profiles begin to resemble power-laws except for the innermost bin which still lies above the power-law (the uncertainty of the best-fit K_0 also increases). The result of a power-law profile with a discrepant central bin is that the degraded K_0 values are only slightly larger than the ~~fiducial~~ best-fit K_0 of the un-degraded data, $(K'_0 - K_0)/K_0 = 0.71 \pm 0.57$.

Our analysis of the degraded entropy profiles suggests that K_0 is more sensitive to the value of $K(r)$ in the central bins than it is to the shape of the profile or the number of radial bins (systematics we explore further in §4.3). Most importantly however, is that low-redshift clusters with $K_0 \leq 10 \text{ keV cm}^2$ look like $K_0 \approx 10 - 30 \text{ keV cm}^2$ ~~clusters~~ at $z > 0.1$. Thus we conclude that the lack of $K_0 < 10 \text{ keV cm}^2$ clusters at $z \gtrsim 0.1$ can be attributed to resolution effects.

4.3. Profile Curvature and Number of Bins

From our analysis of the degraded entropy profiles in §4.2 we found: (1) that the best-fit K_0 is sensitive to the curvature of the entropy profile, and (2) that the number of radial bins may also affect the best-fit K_0 . This raises the possibility of two troubling systematics in our analysis. To check for a possible correlation between best-fit K_0 and profile curvature we first calculated average profile curvatures, κ_A . For each profile, κ_A was calculated using the standard formulation for curvature of a function, $\kappa = \|y''\|/(1+y'^2)^{3/2}$, where we set

$y = K(r) = K_0 + K_{100}(r/100 \text{ kpc})^\alpha$. This derivation yields,

$$\kappa_A = \frac{\int \frac{\|100^{-\alpha}(\alpha-1)\alpha K_{100}r^{\alpha-2}\|}{[1+(100^{-\alpha}\alpha K_{100}r^{\alpha-1})^2]^{3/2}} dr}{\int dr} \quad (6)$$

where α and K_{100} are the best-fit parameters unique to each entropy profile. The integral over all space ensures we evaluate the curvature of each profile in the radial range where the profiles have asymptotically approached a constant at small radii and ~~the~~ a power-law at large radii. We find that at any value of K_0 , a large range of curvatures are covered and that there is no systematic trend in K_0 associated with κ_A .

In §4.2 we also found that profiles with fewer radial bins tend toward lower best-fit K_0 values. After examining figures of the number of bins fit in each entropy profile versus best-fit K_0 we find only scatter and no trends.

We do not find any systematic trends with profile shape or number of fit bins which would significantly effect our best-fit K_0 values. Thus we conclude that the K_0 values presented in the following sections are an adequate measure of the core entropy and any undetected dependence on profile shape or radial resolution affect our results at significance levels much smaller than the measured uncertainties.

5. RESULTS AND DISCUSSION

Presented in Figure 4 is a montage of *ACCEPT* entropy profiles for different temperature ranges. These figures highlight the cornerstone result of *ACCEPT*: a uniformly analyzed collection of entropy profiles covering a broad range of core entropy. Each profile is color-coded ~~in representation~~ of the global cluster temperature. Plotted in each panel of Fig. 4 are the mean profiles representing $K_0 \leq 50 \text{ keV cm}^2$ clusters (dashed-line) and $K_0 > 50 \text{ keV cm}^2$ clusters (dashed-dotted line), in addition to the pure-cooling model of Voit et al. (2002) (solid black line). The theoretical pure-cooling curve represents the entropy profile of a 5 keV cluster simulated with radiative cooling but no feedback. ~~Thus, the curve represents a lower limit of possible entropy distributions and~~ gives us a useful baseline with which to compare *ACCEPT* profiles.

In the following sections we discuss results gleaned from analysis of our library of entropy profiles. ~~Results such as~~ the departure of most entropy profiles from a simple radial power-law profile, the bimodal distribution of core entropy, and the asymptotic convergence of the entropy profiles to the self-similar $K(r) \propto r^{1.1}$ power-law at $r \geq 100 \text{ kpc}$.

5.1. Non-Zero Core Entropy

Arguably the most striking feature of Figure 4 is the departure of most profiles from a simple power-law. Core flattening of surface brightness profiles (and consequently density profiles) is a well known feature of clusters (*e.g.* Mohr et al. 1999 and Xue & Wu 2000). What is notable in our work however is that, based on comparison of reduced χ^2 , very few of the clusters in our sample have an entropy distribution which is best-fit by the power-law only model (eqn. 5), rather they are sufficiently well-described by the model which flattens in the core (eqn. 4).

Of the 233 in *ACCEPT*, only six clusters have a K_0 value which is statistically consistent with zero, or are better fit by the power-law only model: A2151, AS0405, MS 0116.3-0115, and NGC 507 (part of *HIFLUGCS* analysis only). Two clusters, A1991 and A4059, are better fit by the power-law only model when the temperature profile in the core is not

constant (see §3.1). For these six clusters it may be the case that the ICM entropy departs from a power-law at a radial scale smaller than the $5''$ bins we used for extracting surface brightness profiles. After extracting new surface brightness profiles for these six clusters using $2.5''$ bins and repeating the analysis, we find that the profiles for A4059 and AS0405 do flatten. This leaves A1919, A2151, MS 0116.3-0115, and NGC 507 as the only clusters in *ACCEPT* which are statistically well fit by power-laws.

For clusters with central cooling times shorter than the age of the cluster, non-zero core entropy is an expected consequence of episodic heating of the ICM (Voit & Donahue 2005), with AGN as one possible heating source (Bower 1997; Loewenstein 2000; Voit & Bryan 2001; Churazov et al. 2002; Brüggen & Kaiser 2002; Brüggen et al. 2002; Nath & Roychowdhury 2002; Ruszkowski & Begelman 2002; Alexander 2002; Omma et al. 2004; McCarthy et al. 2004; Roychowdhury et al. 2004; Hoeft & Brüggen 2004; Dalla Vecchia et al. 2004; Soker & Pizzolato 2005; Pizzolato & Soker 2005; Brighenti & Mathews 2006; Mathews et al. 2006). Clusters with cooling times of order the age of the Universe, however, require other mechanisms to generate their core entropy, for example ~~via~~ mergers or extremely energetic AGN outbursts. For the very highest K_0 values, $K_0 > 100 \text{ keV cm}^2$, the mechanism by which the core entropy came to be so large is not well understood as it is difficult to boost the entropy of a gas parcel to $> 100 \text{ keV cm}^2$ via merger shocks (McCarthy et al. 2008) and would require AGN outburst energies which have never been observed. We are providing the data and results of *ACCEPT* to the public with the hope that the research community finds it a useful a new resource to further understand the processes which result in non-zero cluster core entropy.

5.2. Bimodality of Core Entropy Distribution

The time required for a gas parcel to radiate away its thermal energy is a function of the gas entropy. Low entropy gas radiates profusely and is thus subject to rapid cooling and vice versa for high entropy gas. Hence, the distribution of K_0 is of particular interest because it is an approximate indicator of the cooling timescale in the cluster core. The K_0 distribution is also interesting because it may be useful in better understanding the physical processes operating in cluster cores. For example, if processes such as thermal conduction and AGN feedback are important in establishing the entropy state of cluster cores, then models which incorporate these processes should approximately reproduce the observed K_0 distribution.

In the top panel of Figure 5 is plotted the logarithmically binned distribution of K_0 . In the bottom panel of Figure 5 is plotted the cumulative distribution of K_0 . One can immediately see from these distributions that there are at least two distinct populations separated by a small number of clusters with $K_0 \approx 40 - 60 \text{ keV cm}^2$. If the distinct bimodality of the K_0 distribution seen in the binned histogram were an artifact of binning, then the cumulative distribution should be relatively smooth. But there are clearly plateaus in the cumulative distribution, with one of these plateaus coincident with the division between the two populations at $K_0 \approx 30 - 60 \text{ keV cm}^2$.

To further test for the presence of a bimodal population we utilized the KMM test of Ashman et al. (1994). The KMM test estimates the probability that a set of data points is better described by the sum of multiple Gaussians than by a single Gaussian. We tested the unimodal case versus the bimodal case, with the assumption that the dispersion of the two Gaus-

sian components are not the same. We have used the updated KMM code of Waters et al. (2008) which incorporates bootstrap resampling to determine uncertainties for all parameters. A post-analysis comparison of fits assuming the populations have the same and different dispersions confirms our initial guess that the dispersions are different is a better model.

The KMM test, as with any statistical test, is very specific. At zeroth order, the KMM test simply determines if a population is unimodal or not, and finds the means of these populations. However, the dispersions of these populations are subject to the quality of sampling and the presence of outliers (*e.g.* KMM must assign all data points to a population). The outputs of the KMM test are the best-fit populations to the data, not necessarily the best-fit populations of the underlying distribution (hence no goodness of fit is output). However, the KMM test does output a P-value, p , and with the assumption that χ^2 describes the distribution of the likelihood ratio statistic, $1 - p$ is the confidence interval for the model considered.

There are a small number of clusters with $K_0 \leq 4 \text{ keV cm}^2$ that when included in the KMM test significantly change the results. Thus we provide two sets of results: results with and without the $K_0 \leq 4 \text{ keV cm}^2$ clusters. The results of the KMM test neglecting $K_0 \leq 4 \text{ keV cm}^2$ clusters were two statistically distinct peaks at $K_1 = 17.8 \pm 6.6 \text{ keV cm}^2$ and $K_2 = 154 \pm 52 \text{ keV cm}^2$. 121 clusters were assigned to the first distribution, while 106 were assigned to the second. Including $K_0 \leq 4 \text{ keV cm}^2$ clusters, the KMM test found populations at $K_1 = 15.0 \pm 5.0 \text{ keV cm}^2$ (89 clusters) and $K_2 = 129 \pm 45 \text{ keV cm}^2$ (131 clusters). The KMM test neglecting $K_0 \leq 4 \text{ keV cm}^2$ clusters returned $p = 1.16 \times 10^{-7}$, while the test including all clusters returned $p = 1.90 \times 10^{-13}$. These tiny p -values indicate the probability the K_0 distribution we observe in our data arises from a single Gaussian population is ~~astoundingly~~ remote.

One possible explanation for a bimodal core entropy distribution is that it arises from the effects of episodic AGN feedback and electron thermal conduction in the cluster core. Voit & Donahue (2005) ~~put forth~~ a model of AGN feedback whereby outbursts of $\sim 10^{45} \text{ ergs s}^{-1}$ occurring every $\sim 10^8 \text{ yrs}$ can maintain a quasi-steady core entropy of $\approx 10 - 30 \text{ keV cm}^2$. In addition, very energetic and infrequent AGN outbursts of 10^{61} ergs can increase the core entropy into the $\approx 30 - 50 \text{ keV cm}^2$ range. This model satisfactorily explains the distribution of $K_0 \lesssim 50 \text{ keV cm}^2$, but depletion of the $K_0 = 30 - 60 \text{ keV cm}^2$ region and populating $K_0 > 60 \text{ keV cm}^2$ requires more physics. Voit et al. (2008) have recently suggested that the dramatic fall-off of clusters beginning at $K_0 \approx 30 \text{ keV cm}^2$ may be the result of electron thermal conduction. After K_0 has ~~gone beyond~~ $K_0 \approx 30 \text{ keV cm}^2$, conduction could severely slow, if not halt, a cluster's core from appreciably cooling and returning to a core entropy state with $K_0 < 30 \text{ keV cm}^2$. This model is supported by results presented in Cavagnolo et al. (2008a), Guo et al. (2008), and Rafferty et al. (2008) which find that the formation of thermal instabilities are extremely sensitive to the core entropy state of a cluster.

We acknowledge that *ACCEPT* is not a complete, uniformly selected sample of clusters. This raises the possibility that our sample is biased towards clusters that have historically drawn the attention of observers, such as cooling flows or mergers. If that were the case, then one reasonable explanation of the K_0 bimodality is that $K_0 = 30 - 60 \text{ keV cm}^2$ clusters are “boring” and thus go unobserved. However, as we show in §5.4, the unbiased flux-limited *HIFLUGCS* sample is also

bimodal. ~~A sociological explanation of bimodality for both ACCEPT and HIFLUGCS is highly unlikely.~~

5.3. The HIFLUGCS Sub-Sample

ACCEPT is not a flux-limited or volume-limited sample. To ensure our results are not affected by an unknown selection bias, we culled the HIFLUGCS sample from ACCEPT for separate analysis. HIFLUGCS is a flux-limited sample ($f_X \geq 2 \times 10^{-11}$ ergs s $^{-1}$ cm $^{-2}$) selected ~~by flux only~~ from the REFLEX sample (Böhringer et al. 2004) with no consideration of morphology. Thus, at any given luminosity in HIFLUGCS there is a good sampling of different morphologies, *i.e.* the bias toward cool-cores or mergers has been removed. The sample also covers most of the sky with holes near Virgo and the Large and Small Magellanic Clouds, and has no known incompleteness (Chen et al. 2007). There are a total of 106 objects in HIFLUGCS: 63 in the primary sample and 43 in the extended sample. Of these 106 objects, no public Chandra observations were available for 16 objects (A548e, A548w, A1775, A1800, A3528n, A3530, A3532, A3560, A3695, A3827, A3888, AS0636, HCG 94, IC 1365, NGC 499, RXCJ 2344.2-0422), 6 objects did not meet our minimum analysis requirements and were thus insufficient for study (3C 129, A1367, A2634, A2877, A3627, Triangulum Australis), and as discussed in §2, Coma and Fornax were intentionally ignored. This left a total of 82 HIFLUGCS objects which we analyzed, 59 from the primary sample ($\sim 94\%$ complete) and 23 from the extended sample ($\sim 50\%$ complete). The primary sample is the more complete of the two, thus we focus our following discussion on the primary sample only.

The clusters missing from the primary HIFLUGCS sample are A1367, A2634, Coma, and Fornax. The extent to which these 4 clusters can change our analysis of the K_0 distribution for HIFLUGCS is limited. To alter or wash-out bimodality, all 4 clusters would need to fall in the range $K_0 = 20 - 40$ keV cm 2 , which is certainly not the case for any of these clusters. Donnelly et al. (1998) find that two sub-clusters are merging in A1367 and that a localized shock has developed. The merger process, and shock heating specifically, are known to create large increases of gas entropy (McCarthy et al. 2007). Given the combination of low surface brightness, moderate temperatures ($kT_X = 3.5 - 5.0$ keV), lack of a temperature gradient, ongoing merger, and presence of a shock, it is unlikely A1367 has a core entropy $\lesssim 50$ keV cm 2 . A2634 is a very low surface brightness cluster with the bright radio source 3C 465 at the center of a compact X-ray source. Clusters with comparable properties to A2634 do not have $K_0 \lesssim 50$ keV cm 2 . Coma and Fornax are known to have core entropy > 60 keV cm 2 (Rafferty et al. 2008).

Shown in Figure 6 are the log-binned (top panel) and cumulative (bottom panel) K_0 distributions of the HIFLUGCS primary sample. The bimodality seen in the full ACCEPT collection is also present in the HIFLUGCS sub-sample. Mean best-fit parameters are given in Table 4. While the gaps do not cover the same K_0 range, it is interesting that both gaps are the deepest around $K_0 \approx 30$ keV cm 2 . That bimodality is present in both ACCEPT and the unbiased HIFLUGCS sub-sample suggests bimodality cannot be the result of simple archival bias.

Hudson & Reiprich (2007) note a similar core entropy bimodality for the to the one we find here. Hudson & Reiprich (2007) discuss two distinct groupings of objects in a plot of average cluster temperature versus core entropy, with the dividing point being $K \approx 40$ keV cm 2 . Our results agree with

the findings of Hudson & Reiprich (2007) with the gap in K_0 occurring at $K_0 \approx 40$ keV cm 2 .

We again performed two KMM tests: one test with, and another test without, clusters having $K_0 \leq 4$ keV cm 2 . For the test including $K_0 \leq 4$ keV cm 2 clusters we find populations at $K_1 = 9.7 \pm 3.5$ keV cm 2 (28 clusters) and $K_2 = 131 \pm 46$ keV cm 2 (31 clusters) with $p = 3.34 \times 10^{-3}$. Excluding clusters with $K_0 \leq 4$ keV cm 2 we find peaks at $K_1 = 10.5 \pm 3.4$ keV cm 2 and $K_2 = 116 \pm 42$ keV cm 2 , each having 21 and 34 clusters, respectively. The probability these populations originate from a unimodal distribution is $p = 1.55 \times 10^{-5}$.

5.4. Distribution of Core Cooling Times

In the X-ray regime, cooling time and entropy are related in that decreasing gas entropy also means shorter cooling time. Thus, if the K_0 distribution is bimodal, the distribution of cooling times should also be bimodal. We have calculated cooling time profiles from the spectral analysis using the relation

$$t_{\text{cool}} = \frac{3nkT_X}{2n_e n_H \Lambda(T, Z)} \quad (7)$$

n is the total ion number ($\approx 2.3n_H$ for a fully ionized plasma), n_e and n_H are the electron and proton densities respectively, $\Lambda(T, Z)$ is the cooling function for a given temperature and metal abundance, and $3/2$ is a constant associated with isochoric cooling. The values of the cooling function, $\Lambda(T, Z)$, were calculated for each temperature profile bin from the flux of the best-fit spectral model using XSPEC. Following the procedure discussed in §3.4, Λ and kT_X were interpolated across the radial grid of the electron density profile. The cooling time profiles were then fit with a simple model analogous to that used for fitting $K(r)$:

$$t_{\text{cool}}(r) = t_{c0} + t_{100} \left(\frac{r}{100 \text{ kpc}} \right)^\alpha \quad (8)$$

where t_{c0} is core cooling time and t_{100} is a normalization at 100 kpc. But the K_0 distribution can also be used to explore the distribution of core cooling times. Assuming free-free interactions are the dominant gas cooling mechanism (*i.e.* $\epsilon \propto T^{1/2}$), Donahue et al. (2005) show that entropy is related to cooling time via the formulation:

$$t_{c0}(K_0) \approx 10^8 \text{ yrs} \left(\frac{K_0}{10 \text{ keV cm}^2} \right)^{3/2} \left(\frac{kT_X}{5 \text{ keV}} \right)^{-1} \quad (9)$$

Shown in Figure 7 is the logarithmically binned and cumulative distributions of best-fit core cooling times from eqn. 8 (top panel) and core cooling times calculated using eqn. 9 (bottom panel). The bin widths in both histograms are 0.20 in log-space. The pile-up of cluster core cooling times below 1 Gyr is well known, *e.g.* (Hu et al. 1985) and more recently Dunn & Fabian (2008), and the cooling times we calculate are consistent with the results of other cooling time studies, *e.g.* Peres et al. (1998) and Rafferty et al. (2008).

Most important about Fig. 7 is that the distinct bimodality of the K_0 distribution is also present in best-fit core cooling time, t_{c0} . A KMM bimodality test for t_{c0} found peaks at $t_{c1} = 0.60 \pm 0.24$ Gyr and $t_{c2} = 6.23 \pm 2.19$ Gyr with 130 and 97 in each respective population. The probability that the unimodal distribution is a better fit is once again exceedingly small, $p = 8.77 \times 10^{-7}$.

But while t_{c0} is bimodal, the gaps in the t_{c0} and $t_{c0}(K_0)$ are offset from each other. The gap in t_{c0} occurs in the range

$\sim 1-2$ Gyrs, while the gap in $t_{c0}(K_0)$ occurs in the range $\sim 0.7-1.0$. It is also interesting that the bimodality in $t_{c0}(K_0)$ is more abrupt and deeper than it is in t_{c0} . The offset gaps and differing sharpness of the two distributions suggests that while bimodality occurs only below a particular cooling time scale ($t_{c0} \lesssim 1$ Gyr), a short core cooling time may not be the fundamental property responsible for bimodality. If entropy is more closely related to the physical processes which cause bimodality than is cooling time, then that the cooling time distribution does not present with the sharp, deep bimodality seen in K_0 suggests entropy is the fundamental quantity related to bimodality.

But, since cooling time profiles are more sensitive to the resolution of the temperature profiles than are the entropy profiles, it may be that resolution effects are limiting the quantification of the true cooling time of the core. For example, if our temperature interpolation scheme is too coarse, or averaging over many small-scale temperature fluctuations significantly increases t_{c0} , then t_{c0} would not be the best approximation of true core cooling time. In which case, the core cooling times might be lower and the sharpness and offsets of the distributions gaps may significantly change.

5.5. Slope and Normalization of Power-law Components

Beyond $r \approx 100$ kpc the entropy profiles show a striking similarity in the slope of the power-law component which is independent of K_0 . For the full sample, the mean value of $\alpha = 1.21 \pm 0.39$. For clusters with $K_0 < 50$ keV cm², the mean $\alpha = 1.20 \pm 0.38$, and for clusters with $K_0 \geq 50$ keV cm², the mean $\alpha = 1.23 \pm 0.40$. A mean slope of $\alpha \approx 1.2$ is not statistically different from the theoretical value of 1.1 found by Tozzi & Norman (2001). For the full sample, the mean value of $K_{100} = 126 \pm 45$ keV cm². Again distinguishing between clusters below and above $K_0 = 50$ keV cm², we find $K_{100} = 150 \pm 50$ keV cm² and $K_{100} = 107 \pm 39$ keV cm², respectively. Scaling each entropy profile by the cluster virial temperature and virial radius considerably reduces the dispersion in K_{100} , but we reserve detailed discussion of scaling relations for a future paper.

6. SUMMARY AND CONCLUSIONS

We have presented intracluster medium entropy profiles for a sample of 233 galaxy clusters (9.66 Msec) taken from the *Chandra* Data Archive. We have named this project *ACCEPT* for “Archive of Chandra Cluster Entropy Profile Tables.” Our analysis software, reduced data products, data tables, figures, cluster images, and results of our analysis for all clusters and observations are freely available at the *ACCEPT* web site: <http://www.pa.msu.edu/astro/MC2/accept>. We encourage observers and theorists to utilize this library of entropy profiles in their own work.

We created radial temperature profiles using spectra extracted from a minimum of three concentric annuli containing 2500 counts each and extending to either the chip edge or $0.5R_{180}$, whichever was smaller. We deprojected surface brightness profiles extracted from $5''$ bins over the energy range 0.7-2.0 keV to obtain the electron gas density as a function of radius. Entropy profiles were calculated from the density and temperature profiles as $K(r) = T(r)n(r)^{-2/3}$. Two models for the entropy distribution were then fit to each profile: a power-law only model (eqn. 5) and a power-law which approaches a constant value at small radii (eqn. 4).

We have demonstrated that the entropy profiles for the majority of *ACCEPT* clusters are best fit by the model which

approaches a constant entropy, K_0 , in the core. The entropy profiles of *ACCEPT* are also remarkably similar at radii greater than 100 kpc, and asymptotically approach the self-similar pure-cooling curve ($r \propto 1.1$) with a slope of $\alpha = 1.21 \pm 0.39$ (the dispersion here is in the sample, not in the uncertainty of the measurement). We also find that the distribution of K_0 for the full archival sample is bimodal with the two populations separated by a poorly populated region at $K_0 \approx 30-60$ keV cm². After culling out the primary *HIFLUGCS* sub-sample of Reiprich (2001); Reiprich & Böhringer (2002), we find the K_0 distribution of this complete sub-sample to be bimodal, refuting the possibility of archival bias.

Two core cooling times were derived for each cluster: (1) cooling time profiles were calculated using eqn. 7 and each cooling time profile was then fit with eqn. 8 returning a best-fit core cooling time, t_{c0} ; (2) Using best-fit K_0 values, entropy was converted to a core cooling time, $t_{c0}(K_0)$ using eqn. 9. We find the distributions of both core cooling times to be bimodal. Comparison of the core cooling times from method (1) and (2) reveals that the gap in the bimodal cooling time distributions occur over different timescales, $\sim 2-3$ Gyrs for t_{c0} , and $\sim 0.7-1$ for $t_{c0}(K_0)$, and that the bimodality of $t_{c0}(K_0)$ is more abrupt. We speculate these two results indicate ICM entropy, and not ICM cooling time, is the fundamental quantity related to bimodality.

After analyzing an ensemble of artificially redshifted entropy profiles, we find the lack of $K_0 \lesssim 10$ keV cm² clusters at $z > 0.1$ is most likely a result of resolution effects. Investigation of possible systematics affecting best-fit K_0 values, such as profile curvature and number of profile bins, revealed no trends which would significantly affect our results. We come to the conclusion that K_0 is an acceptable measure of average core entropy and is not overly influenced by profile shape or radial resolution.

Our results regarding non-zero core entropy and K_0 bimodality fit nicely into the sharpening picture of how feedback and radiative cooling in clusters alter global cluster properties and affect massive galaxy formation. Among the many models of AGN feedback, Voit & Donahue (2005) put forth a model which specifically addresses how AGN outbursts generate and sustain non-zero core entropy in the regime of $K_0 \lesssim 70$ keV cm². In addition, if electron thermal conduction is an important process in clusters, Donahue et al. (2005), Voit & Donahue (2005), and Voit et al. (2008) propose there exists a critical entropy threshold below which conduction is no longer efficient at wiping out thermal instabilities. The consequences of which should be a bimodal core entropy distribution and a sensitivity of cooling by-product formation (like star formation and AGN activity) to this entropy threshold. We show in Cavagnolo et al. (2008a) that indicators of feedback like H α and radio emission are extremely sensitive to the lower-bound of the bimodal gap at $K_0 \approx 30$ keV cm². ~~If mergers and some other unknown mechanism are capable of producing cluster cores with $K_0 > 70$ keV cm² and > 100 keV cm², then taking all of these processes in concert, a closed-loop picture of the ICM's entropy life-cycle is starting to emerge.~~

However, the details are still missing and there are many open questions regarding the evolution of the ICM and formation of thermal instabilities in cluster cores: How are clusters with $K_0 > 100$ keV cm² produced, ~~is fine-tuned pre-heating still the answer?~~ What are the role of MHD instabilities, e.g. MTI (Balbus 2000; Quataert 2008) and HBI (Parrish & Quataert 2008), in shaping the ICM? Are the compact X-ray

sources we find at the cores of some BCGs truly coronae? If so, how did they form and survive in the harsh ICM? And can their properties be used to constrain the effects of conduction? We hope *ACCEPT* will be a useful resource in answering these questions.

K. W. C. thanks Chris Waters for supplying and supporting his new KMM bimodality code. K. W. C. was supported in this work through *Chandra* X-ray Observatory Archive grants AR-6016X and AR-4017A. M. D. acknowledges support from the NASA LTSA program NNG-05GD82G. The *Chandra* X-ray Observatory Center is operated by the Smith-

sonian Astrophysical Observatory for and on behalf of NASA under contract NAS8-03060. This research has made use of software provided by the Chandra X-ray Center in the application packages CIAO, CHIPS, and SHERPA. This research has made use of the NASA/IPAC Extragalactic Database which is operated by the Jet Propulsion Laboratory, California Institute of Technology, under contract with NASA. This research has also made use of NASA's Astrophysics Data System. Some software was obtained from the High Energy Astrophysics Science Archive Research Center, provided by NASA's Goddard Space Flight Center.

REFERENCES

- Alexander, P. 2002, *MNRAS*, 335, 610
- Allen, S. W., & Fabian, A. C. 1998, *MNRAS*, 297, L57
- Anders, E., & Grevesse, N. 1989, *Geochim. Cosmochim. Acta*, 53, 197
- Arnaud, K. A. 1996, in *ASP Conf. Ser. 101: Astronomical Data Analysis Software and Systems V*, ed. G. H. Jacoby & J. Barnes, 17–+
- Arnaud, M., & Evrard, A. E. 1999, *MNRAS*, 305, 631
- Ashman, K. M., Bird, C. M., & Zepf, S. E. 1994, *AJ*, 108, 2348
- Balbus, S. A. 2000, *ApJ*, 534, 420
- Bauer, F. E., Fabian, A. C., Sanders, J. S., Allen, S. W., & Johnstone, R. M. 2005, *MNRAS*, 359, 1481
- Birzan, L., Rafferty, D. A., McNamara, B. R., Wise, M. W., & Nulsen, P. E. J. 2004, *ApJ*, 607, 800
- Böhringer, H., Schuecker, P., Guzzo, L., Collins, C. A., Voges, W., Cruddace, R. G., Ortiz-Gil, A., Chincarini, G., De Grandi, S., Edge, A. C., MacGillivray, H. T., Neumann, D. M., Schindler, S., & Shaver, P. 2004, *A&A*, 425, 367
- Borgani, S., Governato, F., Wadsley, J., Menci, N., Tozzi, P., Quinn, T., Stadel, J., & Lake, G. 2002, *MNRAS*, 336, 409
- Bower, R. G. 1997, *MNRAS*, 288, 355
- Bower, R. G., Benson, A. J., Malbon, R., Helly, J. C., Frenk, C. S., Baugh, C. M., Cole, S., & Lacey, C. G. 2006, *MNRAS*, 370, 645
- Brighenti, F., & Mathews, W. G. 2006, *ApJ*, 643, 120
- Brüggen, M., & Kaiser, C. R. 2002, *Nature*, 418, 301
- Brüggen, M., Kaiser, C. R., Churazov, E., & Enßlin, T. A. 2002, *MNRAS*, 331, 545
- Bryan, G. L., & Norman, M. L. 1998, *ApJ*, 495, 80
- Buote, D. A., & Tsai, J. C. 1996, *ApJ*, 458, 27
- Burns, J. O., Roettiger, K., Pinkney, J., Perley, R. A., Owen, F. N., & Voges, W. 1995, *ApJ*, 446, 583
- Cavagnolo, K. W., Donahue, M., Sun, M., & Voit, G. M. 2008a, *ArXiv e-prints*, arxiv:0806.0382
- Cavagnolo, K. W., Donahue, M., Voit, G. M., & Sun, M. 2008b, *ArXiv e-prints*, arxiv:0803.3858
- Cavaliere, A., & Fusco-Femiano, R. 1978, *A&A*, 70, 677
- Chen, Y., Reiprich, T. H., Böhringer, H., Ikebe, Y., & Zhang, Y.-Y. 2007, *A&A*, 466, 805
- Churazov, E., Sunyaev, R., Forman, W., & Böhringer, H. 2002, *MNRAS*, 332, 729
- Croton, D. J., Springel, V., White, S. D. M., De Lucia, G., Frenk, C. S., Gao, L., Jenkins, A., Kauffmann, G., Navarro, J. F., & Yoshida, N. 2006, *MNRAS*, 365, 11
- Dalla Vecchia, C., Bower, R. G., Theuns, T., Balogh, M. L., Mazzotta, P., & Frenk, C. S. 2004, *MNRAS*, 355, 995
- David, L. P., Jones, C., & Forman, W. 1996, *ApJ*, 473, 692
- Dickey, J. M., & Lockman, F. J. 1990, *ARA&A*, 28, 215
- Donahue, M., Horner, D. J., Cavagnolo, K. W., & Voit, G. M. 2006, *ApJ*, 643, 730
- Donahue, M., Voit, G. M., O'Dea, C. P., Baum, S. A., & Sparks, W. B. 2005, *ApJ*, 630, L13
- Donnelly, R. H., Markevitch, M., Forman, W., Jones, C., David, L. P., Churazov, E., & Gilfanov, M. 1998, *ApJ*, 500, 138
- Dunn, R. J. H., & Fabian, A. C. 2008, *MNRAS*, 385, 757
- Ebeling, H., Edge, A. C., Allen, S. W., Crawford, C. S., Fabian, A. C., & Huchra, J. P. 2000, *MNRAS*, 318, 333
- Ebeling, H., Edge, A. C., Böhringer, H., Allen, S. W., Crawford, C. S., Fabian, A. C., Voges, W., & Huchra, J. P. 1998, *MNRAS*, 301, 881
- Ebeling, H., Edge, A. C., & Henry, J. P. 2001, *ApJ*, 553, 668
- Edge, A. C., & Stewart, G. C. 1991, *MNRAS*, 252, 414
- Edge, A. C., Stewart, G. C., & Fabian, A. C. 1992, *MNRAS*, 258, 177
- Edge, A. C., Stewart, G. C., Fabian, A. C., & Arnaud, K. A. 1990, *MNRAS*, 245, 559
- Eke, V. R., Navarro, J. F., & Frenk, C. S. 1998, *ApJ*, 503, 569
- Ettori, S. 2000, *MNRAS*, 311, 313
- Evrard, A. E. 1997, *MNRAS*, 292, 289
- Evrard, A. E., & Henry, J. P. 1991, *ApJ*, 383, 95
- Evrard, A. E., Metzler, C. A., & Navarro, J. F. 1996, *ApJ*, 469, 494
- Fabian, A. C. 1994, *ARA&A*, 32, 277
- Feretti, L., Böhringer, H., Giovannini, G., & Neumann, D. 1997a, *A&A*, 317, 432
- Feretti, L., Giovannini, G., & Böhringer, H. 1997b, *New Astronomy*, 2, 501
- Finoguenov, A., Reiprich, T. H., & Böhringer, H. 2001, *A&A*, 368, 749
- Gioia, I. M., Maccacaro, T., Schild, R. E., Wolter, A., Stocke, J. T., Morris, S. L., & Henry, J. P. 1990, *ApJS*, 72, 567
- Guo, F., Oh, S. P., & Ruszkowski, M. 2008, *ArXiv e-prints*, arxiv:0804.3823
- Hallman, E. J., Burns, J. O., Motl, P. M., & Norman, M. L. 2007, *ApJ*, 665, 911
- Heckman, T. M., Baum, S. A., van Breugel, W. J. M., & McCarthy, P. 1989, *ApJ*, 338, 48
- Henry, J. P., Mullis, C. R., Voges, W., Böhringer, H., Briel, U. G., Gioia, I. M., & Huchra, J. P. 2006, *ApJS*, 162, 304
- Hoefl, M., & Brüggen, M. 2004, *ApJ*, 617, 896
- Horner, D. J., Mushotzky, R. F., & Scharf, C. A. 1999, *ApJ*, 520, 78
- Hu, E. M., Cowie, L. L., & Wang, Z. 1985, *ApJS*, 59, 447
- Hudson, D. S., & Reiprich, T. H. 2007, in *Heating versus Cooling in Galaxies and Clusters of Galaxies*, ed. H. Böhringer, G. W. Pratt, A. Finoguenov, & P. Schuecker, 42–+
- Hudson, D. S., Reiprich, T. H., Clarke, T. E., & Sarazin, C. L. 2006, *A&A*, 453, 433
- Jeltema, T. E., Canizares, C. R., Bautz, M. W., & Buote, D. A. 2005, *ApJ*, 624, 606
- Jones, C., & Forman, W. 1984, *ApJ*, 276, 38
- Kaast, J. S., Tamura, T., Peterson, J. R., Bleeker, J. A. M., Ferrigno, C., Kahn, S. M., Paerels, F. B. S., Piffaretti, R., Branduardi-Raymont, G., & Böhringer, H. 2004, *A&A*, 413, 415
- Kaiser, N. 1986, *MNRAS*, 222, 323
- Kalberla, P. M. W., Burton, W. B., Hartmann, D., Arnal, E. M., Bajaja, E., Morras, R., & Pöppel, W. G. L. 2005, *A&A*, 440, 775
- Kravtsov, A. V., Vikhlinin, A., & Nagai, D. 2006, *ApJ*, 650, 128
- Kriss, G. A., Cioffi, D. F., & Canizares, C. R. 1983, *ApJ*, 272, 439
- Lloyd-Davies, E. J., Ponman, T. J., & Cannon, D. B. 2000, *MNRAS*, 315, 689
- Loewenstein, M. 2000, *ApJ*, 532, 17
- Loken, C., Norman, M. L., Nelson, E., Burns, J., Bryan, G. L., & Motl, P. 2002, *ApJ*, 579, 571
- Markevitch, M. 1998, *ApJ*, 504, 27
- Mathews, W. G., Faltenbacher, A., & Brighenti, F. 2006, *ApJ*, 638, 659
- Maughan, B. J., Jones, C., Jones, L. R., & Van Speybroeck, L. 2007, *ApJ*, 659, 1125
- McCarthy, I. G., Babul, A., Bower, R. G., & Balogh, M. L. 2008, *MNRAS*, 386, 1309
- McCarthy, I. G., Balogh, M. L., Babul, A., Poole, G. B., & Horner, D. J. 2004, *ApJ*, 613, 811
- McCarthy, I. G., Bower, R. G., Balogh, M. L., Voit, G. M., Pearce, F. R., Theuns, T., Babul, A., Lacey, C. G., & Frenk, C. S. 2007, *MNRAS*, 376, 497
- McNamara, B. R., & Nulsen, P. E. J. 2007, *ARA&A*, 45, 117
- McNamara, B. R., O'Connell, R. W., & Bregman, J. N. 1990, *ApJ*, 360, 20
- Mewe, R., Gronenschild, E. H. B. M., & van den Oord, G. H. J. 1985, *A&AS*, 62, 197

- Mewe, R., Lemen, J. R., & van den Oord, G. H. J. 1986, *A&AS*, 65, 511
- Mohr, J. J., Mathiesen, B., & Evrard, A. E. 1999, *ApJ*, 517, 627
- Molendi, S., de Grandi, S., Fusco-Femiano, R., Colafrancesco, S., Fiore, F., Nesci, R., & Tamburelli, F. 1999, *ApJ*, 525, L73
- Morandi, A., & Etti, S. 2007, *MNRAS*, 380, 1521
- Nagai, D., Kravtsov, A. V., & Vikhlinin, A. 2007, *ApJ*, 668, 1
- Nath, B. B., & Roychowdhury, S. 2002, *MNRAS*, 333, 145
- Navarro, J. F., Frenk, C. S., & White, S. D. M. 1995, *MNRAS*, 275, 720
- . 1997, *ApJ*, 490, 493
- Nevalainen, J., Markevitch, M., & Forman, W. 2000, *ApJ*, 536, 73
- O'Dea, C. P., Baum, S. A., Maloney, P. R., Tacconi, L. J., & Sparks, W. B. 1994, *ApJ*, 422, 467
- O'Hara, T. B., Mohr, J. J., & Guerrero, M. A. 2004, *ApJ*, 604, 604
- Omma, H., Binney, J., Bryan, G., & Slyz, A. 2004, *MNRAS*, 348, 1105
- Parrish, I. J., & Quataert, E. 2008, *ApJ*, 677, L9
- Peres, C. B., Fabian, A. C., Edge, A. C., Allen, S. W., Johnstone, R. M., & White, D. A. 1998, *MNRAS*, 298, 416
- Peterson, J. R., Kahn, S. M., Paerels, F. B. S., Kaastra, J. S., Tamura, T., Bleeker, J. A. M., Ferrigno, C., & Jernigan, J. G. 2003, *ApJ*, 590, 207
- Peterson, J. R., Paerels, F. B. S., Kaastra, J. S., Arnaud, M., Reiprich, T. H., Fabian, A. C., Mushotzky, R. F., Jernigan, J. G., & Sakellou, I. 2001, *A&A*, 365, L104
- Piffaretti, R., Jetzer, P., Kaastra, J. S., & Tamura, T. 2005, *A&A*, 433, 101
- Pizzolato, F., & Soker, N. 2005, *ApJ*, 632, 821
- Ponman, T. J., Cannon, D. B., & Navarro, J. F. 1999, *Nature*, 397, 135
- Ponman, T. J., Sanderson, A. J. R., & Finoguenov, A. 2003, *MNRAS*, 343, 331
- Quataert, E. 2008, *ApJ*, 673, 758
- Rafferty, D., McNamara, B., & Nulsen, P. 2008, *ArXiv e-prints*, arxiv:0802.1864
- Reiprich, T. H. 2001, PhD thesis, AA(Max-Planck-Institut für extraterrestrische Physik, P.O. Box 1312, 85741 Garching, Germany)
- Reiprich, T. H., & Böhringer, H. 2002, *ApJ*, 567, 716
- Rosati, P., della Ceca, R., Burg, R., Norman, C., & Giacconi, R. 1995, *ApJ*, 445, L11
- Roychowdhury, S., Ruszkowski, M., Nath, B. B., & Begelman, M. C. 2004, *ApJ*, 615, 681
- Ruszkowski, M., & Begelman, M. C. 2002, *ApJ*, 581, 223
- Saro, A., Borgani, S., Tornatore, L., Dolag, K., Murante, G., Biviano, A., Calura, F., & Charlot, S. 2006, *MNRAS*, 373, 397
- Sharma, M., McNamara, B. R., Nulsen, P. E. J., Owers, M., Wise, M. W., Blanton, E. L., Sarazin, C. L., Owen, F. N., & David, L. P. 2004, *ApJ*, 613, 180
- Soker, N., & Pizzolato, F. 2005, *ApJ*, 622, 847
- Stewart, G. C., Fabian, A. C., Jones, C., & Forman, W. 1984, *ApJ*, 285, 1
- Sun, M., Jones, C., Forman, W., Vikhlinin, A., Donahue, M., & Voit, M. 2007, *ApJ*, 657, 197
- Sun, M., Voit, G. M., Donahue, M., Jones, C., & Forman, W. 2008, *ArXiv e-prints*, arxiv:0805.2320
- Tamura, T., Kaastra, J. S., Peterson, J. R., Paerels, F. B. S., Mittaz, J. P. D., Trudolyubov, S. P., Stewart, G., Fabian, A. C., Mushotzky, R. F., Lumb, D. H., & Ikebe, Y. 2001, *A&A*, 365, L87
- Teyssier, R., Chieze, J.-P., & Alimi, J.-M. 1997, *ApJ*, 480, 36
- Tozzi, P., & Norman, C. 2001, *ApJ*, 546, 63
- Ventimiglia, D. A., Voit, G. M., Donahue, M., & Ameglio, S. 2008, *ArXiv e-prints*, arxiv:0806.0850
- Vikhlinin, A., Markevitch, M., Murray, S. S., Jones, C., Forman, W., & Van Speybroeck, L. 2005, *ApJ*, 628, 655
- Vikhlinin, A., McNamara, B. R., Forman, W., Jones, C., Quintana, H., & Hornstrup, A. 1998, *ApJ*, 502, 558
- Voit, G. M., & Bryan, G. L. 2001, *Nature*, 414, 425
- Voit, G. M., Bryan, G. L., Balogh, M. L., & Bower, R. G. 2002, *ApJ*, 576, 601
- Voit, G. M., Cavagnolo, K. W., Donahue, M., Rafferty, D. A., McNamara, B. R., & Nulsen, P. E. J. 2008, *ApJ*, 681, L5
- Voit, G. M., & Donahue, M. 1995, *ApJ*, 452, 164
- . 2005, *ApJ*, 634, 955
- Wang, Q. D., Connolly, A., & Brunner, R. 1997, *ApJ*, 487, L13+
- Wang, Q. D., Owen, F., & Ledlow, M. 2004, *ApJ*, 611, 821
- Waters, C. Z., Zepf, S. E., Lauer, T. R., & Baltz, E. A. 2008, *Submitted to ApJ*
- White, D. A., Jones, C., & Forman, W. 1997, *MNRAS*, 292, 419
- Xue, Y.-J., & Wu, X.-P. 2000, *MNRAS*, 318, 715

APPENDIX

NOTES ON CLUSTERS REQUIRING β -MODEL FIT

NB: In this section we abbreviate surface brightness as SB.

Abell 119 ($z = 0.0442$): This is a highly diffuse cluster without a prominent cool core. The large core region and slowly varying SB made deprojection highly unstable. We have excluded a small source at the very center of the BCG. The exclusion region for the source is $\approx 2.2''$ in radius which at the redshift of the cluster is ~ 2 kpc. This cluster required a double β -model.

Abell 160 ($z = 0.0447$): The highly asymmetric, low SB of this cluster resulted in a noisy surface brightness profile that could not be deprojected. This cluster required a double β -model. The BCG hosts a compact X-ray source. The exclusion region for the compact source has a radius of $\sim 5''$ or ~ 4.3 kpc. The BCG for this cluster is not coincident with the X-ray centroid and hence is not at the zero-point of our radial analysis.

Abell 193 ($z = 0.0485$): This cluster has an azimuthally symmetric and a very diffuse ICM centered on a BCG which is interacting with a companion galaxy. In Fig. 1 one can see that the central three bins of this cluster's SB profile are highly discrepant from the best-fit β -model. This is a result of the BCG being coincident with a bright, compact X-ray source. As we have concluded in 3.5, compact X-ray sources are excluded from our analysis as they are not the focus of our study here. Hence we have used the best-fit β -model in deriving $K(r)$ instead of the raw SB.

Abell 400 ($z = 0.0240$): The two ellipticals at the center of this cluster have compact X-ray sources which are excluded during analysis. The core entropy we derive for this cluster is in agreement with that found by Hudson et al. (2006) which supports the accuracy of the β -model we have used.

Abell 1060 ($z = 0.0125$): There is a distinct compact source associated with the BCG in this cluster. The ICM is also very faint and uniform in surface brightness making the compact source that much more obvious. Deprojection was unstable because of imperfect exclusion of the source.

Abell 1240 ($z = 0.1590$): The SB of this cluster is well-modeled by a β -model. There is nothing peculiar worth noting about the BCG or the core of this cluster.

Abell 1736 ($z = 0.0338$): Another "boring" cluster with a very diffuse low SB ICM, no peaky core, and no signs of merger activity in the X-ray. The noisy SB profile necessitated the use of a double β -model. The BCG is coincident with a very compact X-ray source, but the BCG is offset from the X-ray centroid and thus the central bins are not adversely affected. The radius of the exclusion region for the compact source is $\approx 2.3''$ or 1.5 kpc.

Abell 2125 ($z = 0.2465$): Although the ICM of this cluster is very similar to the other clusters listed here (*i.e.* diffuse, large cores), A2125 is one of the more compact clusters. The presence of several merging sub-clusters (Wang et al. 1997, 2004) to the NW of the main cluster form a diffuse mass which cannot rightly be excluded. This complication yields inversions of the deprojected SB profile if a double β -model is not used.

Abell 2255 ($z = 0.0805$): This is a very well studied merger cluster (Burns et al. 1995; Feretti et al. 1997a). The core of this cluster is very large ($r > 200$ kpc). Such large extended cores cannot be deprojected using our methods because if too many neighboring bins have approximately the same SB, deprojection results in bins with negative or zero value. The SB for this cluster is well modeled as a β function.

Abell 2319 ($z = 0.0562$): A2319 is another well studied merger cluster (Feretti et al. 1997b; Molendi et al. 1999) with a very large core region ($r > 100$ kpc) and a prominent cold front (O'Hara et al. 2004). Once again, the SB profile is well-fit by a β -model.

Abell 2462 ($z = 0.0737$): This cluster is very similar in appearance to A193: highly symmetric ICM with a bright, compact X-ray source embedded at the center of an extended diffuse ICM. The central compact source has been excluded from our analysis with a region of radius $\approx 1.5''$ or ~ 3 kpc. The central bin of the SB profile is most likely boosted above the best-fit double β -model because of faint extended emission from the compact source which cannot be discerned from the ambient ICM.

Abell 2631 ($z = 0.2779$): The SB profile for this cluster is rather regular, but because the cluster has a large core it suffers from the same unstable deprojection as A2255 and A2319. The ICM is symmetric about the BCG and is incredibly uniform in the core region. We did not detect or exclude a source at the center of this cluster, but under heavy binning the cluster image appears to have a source coincident with the BCG, and the slightly higher flux in central bin of the SB profile may be a result of an unresolved source.

Abell 3376 ($z = 0.0456$): The large core of this cluster ($r > 120$ kpc) makes deprojection unstable and a β -model must be used.

Abell 3391 ($z = 0.0560$): The BCG is coincident with a compact X-ray source. The source is excluded using a region with radius $\approx 2''$ or ~ 2 kpc. The large uniform core region made deprojection unstable and thus required a β -model fit.

Abell 3395 ($z = 0.0510$): The SB profile for this cluster is noisy resulting in deprojection inversions and requiring a β -model fit. The BCG of this cluster has a compact X-ray source and this source was excluded using a region with radius $\approx 1.9''$ or ~ 2 kpc.

MKW 08 ($z = 0.0270$): MKW 08 is a nearby large group/poor cluster with a pair of interacting elliptical galaxies in the core. The BCG falls directly in the middle of the ACIS-I detector gap. However, despite the lack of proper exposure, CCD dithering reveals that a very bright X-ray source is associated with the BCG. A double β -model was necessary for this cluster because the low SB of the ICM is noisy and deprojection is unstable.

RBS 461 ($z = 0.0290$): This is another nearby large group/poor cluster with an extended, diffuse, axisymmetric, featureless ICM centered on the BCG. The BCG is coincident with a compact source with size $r \approx 1.7$ kpc. This source was excluded during reduction. The β -model is a good fit to the SB profile.

TABLE 1
SUMMARY OF SAMPLE

Cluster	Obs. ID	R.A.	Decl.	Exposure Time	ACIS	z	kT_X	$L_{bol.}$	Notes
—	—	hr:min:sec	° : ' : ''	ksec	—	—	keV	10^{44} ergs s $^{-1}$	—
(1)	(2)	(3)	(4)	(5)	(6)	(7)	(8)	(9)	(10)
1E0657 56	3184	06:58:29.627	-55:56:39.79	87.5	I3	0.2960	11.64	52.50	—
—	5356	—	—	97.2	I2	—	—	—	—
—	5361	—	—	82.6	I3	—	—	—	—
2A 335+096	919	03:38:41.105	+09:58:00.66	19.7	S3	0.0347	2.88	9.77	—
2PIGG J0011.5-2850	5797	00:11:21.623	-28:51:14.44	19.9	I3	0.0753	5.15	2.17	f
2PIGG J2227.0-3041	5798	22:27:54.560	-30:34:34.84	22.3	I2	0.0729	2.79	0.81	—
3C 28.0	3233	00:55:50.401	+26:24:36.47	49.7	I3	0.1952	5.53	4.83	—
3C 295	2254	14:11:20.280	+52:12:10.55	90.9	I3	0.4641	5.16	7.01	d
3C 388	5295	18:44:02.365	+45:33:29.31	30.7	I3	0.0917	3.23	0.53	d
4C 55.16	4940	08:34:54.923	+55:34:21.15	96.0	S3	0.2420	4.98	5.97	d
Abell 13	4945	00:13:37.883	-19:30:09.10	55.3	S3	0.0940	6.84	1.42	—
Abell 68	3250	00:37:06.475	+09:09:32.28	10.0	I3	0.2546	9.01	12.80	—
Abell 85	904	00:41:50.406	-09:18:10.79	38.4	I0	0.0558	6.40	5.30	—
Abell 119	4180	00:56:15.150	-01:14:59.70	11.9	I3	0.0442	5.86	1.41	a,e
Abell 133	2203	01:02:41.756	-21:52:49.79	35.5	S3	0.0558	4.31	0.83	—
Abell 160	3219	01:13:00.692	+15:29:15.08	58.5	I3	0.0447	2.70	-0.00	a,e
Abell 193	6931	01:25:07.660	+08:41:57.08	17.9	S3	0.0485	2.50	-0.00	a,e
Abell 209	3579	01:31:52.565	-13:36:38.79	10.0	I3	0.2060	8.28	11.00	—
—	522	—	—	10.0	I3	—	—	—	—
Abell 222	4967	01:37:34.562	-12:59:34.88	45.1	I3	0.2130	4.60	10.50	—
Abell 223	49671	01:37:55.963	-12:49:10.53	45.1	I0	0.2070	5.28	11.20	e
Abell 262	2215	01:52:46.299	+36:09:11.80	28.7	S3	0.0164	2.18	1.05	—
—	7921	—	—	110.7	S3	—	—	—	—
Abell 267	1448	01:52:42.269	+01:00:45.33	7.9	I3	0.2300	6.79	8.62	—
—	3580	—	—	19.9	I3	—	—	—	—
Abell 368	9412	02:37:27.640	-26:30:28.99	18.4	I3	0.2200	5.62	-0.00	—
Abell 370	515	02:39:53.169	-01:34:36.96	88.0	S3	0.3747	7.35	12.10	—
Abell 383	2321	02:48:03.364	-03:31:44.69	19.5	S3	0.1871	4.91	5.39	—
Abell 399	3230	02:57:53.382	+13:01:30.86	48.6	I0	0.0716	7.95	4.40	—
Abell 400	4181	02:57:41.603	+06:01:27.61	21.5	I3	0.0240	2.31	0.85	a,e
Abell 401	2309	02:58:56.920	+13:34:14.51	11.6	I2	0.0745	8.07	8.39	—
—	518	—	—	18.0	I3	—	—	—	—
Abell 426	3209	03:19:48.194	+41:30:40.73	95.8	S3	0.0179	3.55	50.00	d
—	4289	—	—	95.4	S3	—	—	—	—
Abell 478	1669	04:13:25.345	+10:27:55.15	42.4	S3	0.0883	7.07	16.40	—
—	6102	—	—	10.0	I3	—	—	—	—
Abell 496	3361	04:33:38.038	-13:15:39.65	10.0	S3	0.0328	5.03	0.57	—
Abell 520	4215	04:54:10.303	+02:55:36.48	66.3	I3	0.2020	9.29	13.10	—
Abell 521	430	04:54:06.337	-10:13:16.88	39.1	S3	0.2533	7.03	9.85	—
Abell 539	5808	05:16:37.335	+06:26:25.18	24.3	I3	0.0288	3.24	1.82	b,e
—	7209	—	—	18.6	I3	—	—	—	—
Abell 562	6936	06:53:21.524	+69:19:51.19	51.5	S3	0.1100	3.04	2.14	e
Abell 576	3289	07:21:30.394	+55:45:41.95	38.6	S3	0.0385	4.43	0.47	e
Abell 586	530	07:32:20.339	+31:37:58.59	10.0	I3	0.1710	6.47	8.61	—
Abell 611	3194	08:00:56.832	+36:03:24.09	36.1	S3	0.2880	7.06	10.90	e
Abell 644	2211	08:17:25.225	-07:30:40.03	29.7	I3	0.0698	7.73	7.61	—
Abell 665	3586	08:30:59.226	+65:50:20.06	29.7	I3	0.1810	7.45	13.50	—
Abell 697	4217	08:42:57.549	+36:21:57.65	19.5	I3	0.2820	9.52	26.30	—
Abell 744	6947	09:07:20.455	+16:39:06.18	39.5	I3	0.0729	2.50	0.89	e
Abell 754	577	09:09:18.188	-09:41:09.56	44.2	I3	0.0543	9.94	33.10	—
Abell 773	5006	09:17:52.566	+51:43:38.18	19.8	I3	0.2170	7.83	13.00	—
Abell 907	3185	09:58:21.946	-11:03:50.73	48.0	I3	0.1527	5.59	6.25	—
—	3205	—	—	47.1	I3	—	—	—	—
—	535	—	—	11.0	I3	—	—	—	—
Abell 963	903	10:17:03.744	+39:02:49.17	36.3	S3	0.2056	6.73	10.70	—
Abell 1060	2220	10:36:42.828	-27:31:42.06	31.9	I3	0.0125	3.29	0.01	a,e,f
Abell 1063S	4966	22:48:44.294	-44:31:48.37	26.7	I3	0.3540	11.96	71.50	—
Abell 1068	1652	10:40:44.520	+39:57:10.28	26.8	S3	0.1375	4.62	4.77	—
Abell 1201	4216	11:12:54.489	+13:26:08.76	39.7	S3	0.1688	5.61	4.08	—
Abell 1204	2205	11:13:20.419	+17:35:38.45	23.6	I3	0.1706	3.63	3.98	—
Abell 1240	4961	11:23:38.357	+43:05:48.33	51.3	I3	0.1590	4.77	-0.00	a
Abell 1361	2200	11:43:39.637	+46:21:20.41	16.7	S3	0.1171	5.32	2.39	—
Abell 1413	5003	11:55:17.893	+23:24:21.84	75.1	I2	0.1426	7.41	10.20	—
Abell 1423	538	11:57:17.263	+33:36:37.44	9.8	I3	0.2130	6.01	7.07	—
Abell 1446	4975	12:02:03.744	+58:02:17.93	58.4	S3	0.1035	4.00	-0.00	—
Abell 1569	6100	12:36:26.015	+16:32:17.81	41.2	I3	0.0735	2.51	-0.00	—
Abell 1644	2206	12:57:11.665	-17:24:32.86	18.7	I3	0.0471	4.60	-0.00	b
—	7922	—	—	51.5	I3	—	—	—	—
Abell 1650	4178	12:58:41.499	-01:45:44.32	27.3	S3	0.0843	6.17	4.37	—
Abell 1651	4185	12:59:22.830	-04:11:45.86	9.6	I3	0.0840	6.26	6.71	—
Abell 1664	1648	13:03:42.622	-24:14:41.59	9.8	S3	0.1276	4.39	3.14	—
—	7901	—	—	36.6	S3	—	—	—	—
Abell 1689	1663	13:11:29.612	-01:20:28.69	10.7	I3	0.1843	10.10	24.70	—
—	5004	—	—	19.9	I3	—	—	—	—

TABLE 1 — *Continued*

Cluster — (1)	Obs. ID — (2)	R.A. hr:min:sec (3)	Decl. ° : ' : '' (4)	Exposure Time ksec (5)	ACIS — (6)	z — (7)	kT_X keV (8)	$L_{bol.}$ 10^{44} ergs s $^{-1}$ (9)	Notes — (10)
—	540	—	—	10.3	I3	—	—	—	—
Abell 1736	4186	13:26:49.453	-27:09:48.13	14.9	I1	0.0338	3.45	3.47	a,e
Abell 1758	2213	13:32:48.398	+50:32:32.53	58.3	S3	0.2792	12.14	21.10	—
Abell 1763	3591	13:35:17.957	+40:59:55.80	19.6	I3	0.1866	7.78	9.33	—
Abell 1795	493	13:48:52.802	+26:35:23.55	19.6	S3	0.0625	7.80	7.59	—
—	5289	—	—	15.0	I3	—	—	—	—
Abell 1835	495	14:01:01.951	+02:52:43.18	19.5	S3	0.2532	9.77	39.60	—
Abell 1914	3593	14:26:03.060	+37:49:27.84	18.9	I3	0.1712	9.62	26.40	—
Abell 1942	3290	14:38:21.878	+03:40:12.97	57.6	I2	0.2240	4.77	2.30	—
Abell 1991	3193	14:54:31.620	+18:38:41.48	38.3	S3	0.0587	2.67	0.45	—
Abell 1995	7021	14:52:57.410	+58:02:56.84	48.5	I3	0.3186	3.40	38.00	—
Abell 2029	4977	15:10:56.139	+05:44:40.47	77.9	S3	0.0765	7.38	58.90	—
—	6101	—	—	9.9	I3	—	—	—	—
—	891	—	—	19.8	S3	—	—	—	—
Abell 2034	2204	15:10:12.498	+33:30:39.57	53.9	I3	0.1130	7.15	6.50	f
Abell 2052	5807	15:16:44.514	+07:01:17.02	127.0	S3	0.0353	2.98	5.13	d
—	890	—	—	36.8	S3	—	—	—	—
Abell 2063	4187	15:23:04.851	+08:36:20.16	8.8	I3	0.0351	3.61	4.27	—
—	6263	—	—	16.8	S3	—	—	—	—
Abell 2065	31821	15:22:29.517	+27:42:22.93	27.7	I3	0.0730	5.75	2.95	—
Abell 2069	4965	15:24:11.376	+29:52:19.02	55.4	I2	0.1160	6.50	3.85	—
Abell 2104	895	15:40:08.131	-03:18:15.02	49.2	S3	0.1554	8.53	6.98	—
Abell 2107	4960	15:39:39.113	+21:46:57.66	35.6	I3	0.0411	3.82	3.02	b
Abell 2111	544	15:39:40.637	+34:25:28.01	10.3	I3	0.2300	7.13	7.51	—
Abell 2124	3238	15:44:59.131	+36:06:34.11	19.4	S3	0.0658	4.73	0.46	—
Abell 2125	2207	15:41:14.154	+66:15:57.20	81.5	I3	0.2465	2.88	0.79	a
Abell 2142	1196	15:58:20.880	+27:13:44.21	11.4	S3	0.0898	8.24	75.90	—
—	1228	—	—	12.1	S3	—	—	—	—
—	5005	—	—	44.6	I3	—	—	—	—
Abell 2147	3211	16:02:17.025	+15:58:28.32	17.9	I3	0.0356	4.09	0.73	—
Abell 2151	4996	16:04:35.887	+17:43:17.36	21.8	I3	0.0366	2.90	1.41	e
Abell 2163	1653	16:15:45.705	-06:09:00.62	71.1	I1	0.1695	19.20	49.30	—
Abell 2199	497	16:28:38.249	+39:33:04.28	19.5	S3	0.0300	4.55	0.81	b
Abell 2204	499	16:32:46.920	+05:34:32.86	10.1	S3	0.1524	6.97	22.00	—
—	6104	—	—	9.6	I3	—	—	—	—
—	7940	—	—	77.1	I3	—	—	—	—
Abell 2218	1666	16:35:50.831	+66:12:42.31	48.6	I0	0.1713	7.35	8.46	—
Abell 2219	896	16:40:20.112	+46:42:42.84	42.3	S3	0.2256	12.75	38.30	—
Abell 2244	4179	17:02:42.579	+34:03:37.34	57.0	S3	0.0967	5.68	5.54	—
Abell 2255	894	17:12:42.935	+64:04:10.81	39.4	I3	0.0805	6.12	3.70	a
Abell 2256	1386	17:03:44.567	+78:38:11.51	12.4	I3	0.0579	6.90	25.70	a
Abell 2259	3245	17:20:08.299	+27:40:11.53	10.0	I3	0.1640	5.18	5.43	—
Abell 2261	5007	17:22:27.254	+32:07:58.60	24.3	I3	0.2240	7.63	17.60	—
Abell 2294	3246	17:24:10.149	+85:53:09.77	10.0	I3	0.1780	9.98	10.40	—
Abell 2319	3231	19:21:09.638	+43:57:21.53	14.4	I1	0.0562	10.87	12.70	a
Abell 2384	4202	21:52:21.178	-19:32:51.90	31.5	I3	0.0945	4.75	1.98	—
Abell 2390	4193	21:53:36.825	+17:41:44.38	95.1	S3	0.2301	11.15	35.60	—
Abell 2409	3247	22:00:52.567	+20:58:06.55	10.2	I3	0.1479	5.94	7.08	—
Abell 2420	8271	22:10:18.792	-12:10:13.35	8.1	I3	0.0846	7.89	-0.00	—
Abell 2462	4159	22:39:11.367	-17:20:28.33	39.2	S3	0.0737	2.50	-0.00	a,e
Abell 2537	4962	23:08:22.313	-02:11:29.88	36.2	S3	0.2950	8.40	10.20	—
Abell 2554	1696	23:12:19.622	-21:30:11.32	19.9	S3	0.1103	5.29	1.66	—
Abell 2556	2226	23:13:01.413	-21:38:04.47	19.9	S3	0.0862	3.50	1.53	—
Abell 2589	3210	23:23:57.315	+16:46:38.43	13.7	S3	0.0415	3.65	0.33	—
Abell 2597	922	23:25:19.779	-12:07:27.63	39.4	S3	0.0854	4.02	1.47	—
Abell 2626	3192	23:36:30.452	+21:08:47.36	24.8	S3	0.0573	3.29	0.66	—
Abell 2631	3248	23:37:38.560	+00:16:05.02	9.2	I3	0.2779	7.06	12.70	a
Abell 2657	4941	23:44:57.253	+09:11:30.74	16.1	I3	0.0402	3.77	4.27	—
Abell 2667	2214	23:51:39.395	-26:05:02.75	9.6	S3	0.2300	6.75	20.10	—
Abell 2717	6974	00:03:12.968	-35:56:00.13	19.8	I3	0.0475	1.69	0.26	e
Abell 2744	2212	00:14:19.529	-30:23:30.24	24.8	S3	0.3080	9.18	29.20	—
—	7915	—	—	18.6	I3	—	—	—	—
—	8477	—	—	45.9	I3	—	—	—	—
—	8557	—	—	27.8	I3	—	—	—	—
Abell 2813	9409	00:43:24.881	-20:37:25.08	19.9	I3	0.2924	8.39	-0.00	—
Abell 3084	9413	03:04:03.920	-36:56:27.17	19.9	I3	0.0977	4.56	-0.00	—
Abell 3088	9414	03:07:01.734	-28:39:55.47	18.9	I3	0.2534	6.71	38.90	—
Abell 3112	2516	03:17:57.681	-44:14:17.16	16.9	S3	0.0720	5.17	3.28	d
Abell 3120	6951	03:21:56.464	-51:19:35.40	26.8	I3	0.0690	4.39	-0.00	—
Abell 3158	3201	03:42:54.675	-53:37:24.36	24.8	I3	0.0580	4.94	3.45	—
—	3712	—	—	30.9	I3	—	—	—	—
Abell 3266	899	04:31:13.304	-61:27:12.59	29.8	I1	0.0590	9.07	2.77	—
Abell 3364	9419	05:47:37.698	-31:52:23.61	19.8	I3	0.1483	6.59	-0.00	—
Abell 3376	3202	06:02:11.756	-39:56:59.07	44.3	I3	0.0456	4.08	0.75	a
—	3450	—	—	19.8	I3	—	—	—	—

TABLE 1 — *Continued*

Cluster — (1)	Obs. ID — (2)	R.A. hr:min:sec (3)	Decl. ° : ' : '' (4)	Exposure Time ksec (5)	ACIS — (6)	z — (7)	kT_X keV (8)	$L_{bol.}$ 10^{44} ergs s $^{-1}$ (9)	Notes — (10)
Abell 3391	4943	06:26:21.511	-53:41:44.81	18.4	I3	0.0560	6.07	1.44	a,e
Abell 3395	4944	06:26:48.463	-54:32:59.21	21.9	I3	0.0510	5.13	5.75	a,e
Abell 3528S	8268	12:54:40.897	-29:13:38.10	8.1	I3	0.0530	4.94	-0.00	—
Abell 3558	1646	13:27:56.854	-31:29:43.78	14.4	S3	0.0480	6.60	1.62	e,f
Abell 3562	4167	13:33:37.800	-31:40:12.04	19.3	I2	0.0490	4.59	1.11	—
Abell 3571	4203	13:47:28.434	-32:51:52.45	34.0	S3	0.0391	7.77	1.25	—
Abell 3581	1650	14:07:29.777	-27:01:05.88	7.2	S3	0.0218	2.10	1.23	d
Abell 3667	5751	20:12:41.231	-56:50:35.70	128.9	I3	0.0556	6.51	4.25	—
—	5752	—	—	60.4	I3	—	—	—	—
—	5753	—	—	103.6	I3	—	—	—	—
—	889	—	—	50.3	I2	—	—	—	—
Abell 3822	8269	21:54:04.203	-57:52:02.71	8.1	I3	0.0759	5.45	-0.00	e
Abell 3921	4973	22:49:57.829	-64:25:42.17	29.4	I3	0.0927	5.69	3.37	—
Abell 4038	4992	23:47:43.180	-28:08:34.81	33.5	I2	0.0300	3.11	0.82	—
Abell 4059	5785	23:57:01.065	-34:45:33.28	92.1	S3	0.0475	4.69	6.76	—
Abell S0405	8272	03:51:32.815	-82:13:10.19	7.9	I3	0.0613	4.63	-0.00	—
Abell S0592	9420	06:38:48.610	-53:58:26.32	19.9	I3	0.2216	8.24	-0.00	—
AC 114	1562	22:58:48.316	-34:48:08.20	72.5	S3	0.3120	7.53	11.00	—
AWM7	908	02:54:27.631	+41:34:47.07	47.9	I3	0.0172	3.71	4.07	b
Centaurus	4190	12:48:49.267	-41:18:39.54	34.3	S3	0.0109	3.96	1.74	b
—	4191	—	—	34.0	S3	—	—	—	—
—	4954	—	—	89.1	S3	—	—	—	—
—	4955	—	—	44.7	S3	—	—	—	—
—	504	—	—	31.8	S3	—	—	—	—
—	505	—	—	10.0	S3	—	—	—	—
—	5310	—	—	49.3	S3	—	—	—	—
CID 72	2018	17:33:03.247	+43:45:37.28	30.7	S3	0.0344	2.88	-0.00	—
—	6949	—	—	38.6	I3	—	—	—	—
—	7321	—	—	37.5	I3	—	—	—	—
—	7322	—	—	37.5	I3	—	—	—	—
CL J1226.9+3332	3180	12:26:58.373	+33:32:47.36	31.7	I3	0.8900	10.00	30.80	—
—	5014	—	—	32.7	I3	—	—	—	—
—	932	—	—	9.8	S3	—	—	—	—
Cygnus A	360	19:59:28.381	+40:44:01.98	34.7	S3	0.0561	7.68	2.18	d
ESO 3060170	3188	05:40:06.687	-40:50:12.82	14.0	I3	0.0358	2.79	0.66	b
—	3189	—	—	14.1	I0	—	—	—	—
ESO 5520200	3206	04:54:52.318	-18:06:56.52	23.9	I3	0.0314	2.37	0.09	—
EXO 422-086	4183	04:25:51.271	-08:33:36.42	10.0	I3	0.0397	3.40	0.74	—
HCG 62	921	12:53:05.741	-09:12:15.64	48.5	S3	0.0146	1.10	0.08	—
HCG 42	3215	10:00:14.234	-19:38:10.77	31.7	S3	0.0133	0.70	0.02	—
Hercules A	1625	16:51:08.161	+04:59:32.44	14.8	S3	0.1541	5.21	3.48	—
—	5796	—	—	47.5	S3	—	—	—	—
—	6257	—	—	49.5	S3	—	—	—	—
Hydra A	4970	09:18:05.985	-12:05:43.94	98.8	S3	0.0549	4.00	2.63	d
—	576	—	—	19.5	S3	—	—	—	—
M49	321	12:29:46.841	+08:00:01.98	39.6	S3	0.0033	1.33	-0.00	c
M87	5826	12:30:49.383	+12:23:28.67	126.8	I3	0.0044	2.50	-0.00	d
—	5827	—	—	156.2	I3	—	—	—	—
MACS J0011.7-1523	3261	00:11:42.965	-15:23:20.79	21.6	I3	0.3600	5.42	10.80	—
—	6105	—	—	37.3	I3	—	—	—	—
MACS J0035.4-2015	3262	00:35:26.573	-20:15:46.06	21.4	I3	0.3644	7.39	19.80	—
MACS J0159.8-0849	3265	01:59:49.453	-08:50:00.90	17.9	I3	0.4050	9.59	26.30	—
—	6106	—	—	35.3	I3	—	—	—	—
MACS J0242.5-2132	3266	02:42:35.906	-21:32:26.30	11.9	I3	0.3140	5.58	12.90	—
MACS J0257.1-2325	1654	02:57:09.130	-23:26:05.85	19.8	I3	0.5053	10.50	21.70	—
—	3581	—	—	18.5	I3	—	—	—	—
MACS J0257.6-2209	3267	02:57:41.024	-22:09:11.12	20.5	I3	0.3224	8.02	10.90	—
MACS J0308.9+2645	3268	03:08:55.927	+26:45:38.34	24.4	I3	0.3240	10.54	20.60	—
MACS J0329.6-0211	3257	03:29:41.681	-02:11:47.67	9.9	I3	0.4500	5.20	12.80	—
—	3582	—	—	19.9	I3	—	—	—	—
—	6108	—	—	39.6	I3	—	—	—	—
MACS J0417.5-1154	3270	04:17:34.686	-11:54:32.71	12.0	I3	0.4400	11.07	38.20	—
MACS J0429.6-0253	3271	04:29:36.088	-02:53:09.02	23.2	I3	0.3990	5.66	11.70	—
MACS J0520.7-1328	3272	05:20:42.052	-13:28:49.38	19.2	I3	0.3398	6.27	9.63	—
MACS J0547.0-3904	3273	05:47:01.582	-39:04:28.24	21.7	I3	0.2100	3.58	1.62	e
MACS J0717.5+3745	1655	07:17:31.654	+37:45:18.52	19.9	I3	0.5480	10.50	46.60	—
—	4200	—	—	59.2	I3	—	—	—	—
MACS J0744.8+3927	3197	07:44:52.802	+39:27:24.41	20.2	I3	0.6860	11.29	24.70	—
—	3585	—	—	19.9	I3	—	—	—	—
—	6111	—	—	49.5	I3	—	—	—	—
MACS J1115.2+5320	3253	11:15:15.632	+53:20:03.31	8.8	I3	0.4390	8.03	14.30	—
—	5008	—	—	18.0	I3	—	—	—	—
—	5350	—	—	6.9	I3	—	—	—	—
MACS J1115.8+0129	3275	11:15:52.048	+01:29:56.56	15.9	I3	0.1200	6.78	1.49	—
MACS J1131.8-1955	3276	11:31:54.580	-19:55:44.54	13.9	I3	0.3070	8.64	17.60	—

TABLE 1 — *Continued*

Cluster — (1)	Obs. ID — (2)	R.A. hr:min:sec (3)	Decl. ° : ' : '' (4)	Exposure Time ksec (5)	ACIS — (6)	z — (7)	kT_X keV (8)	$L_{bol.}$ 10^{44} ergs s $^{-1}$ (9)	Notes — (10)
MACS J1149.5+2223	1656	11:49:35.856	+22:23:55.02	18.5	I3	0.5440	8.40	21.60	—
—	3589	—	—	20.0	I3	—	—	—	—
MACS J1206.2-0847	3277	12:06:12.276	-08:48:02.40	23.5	I3	0.4400	10.21	37.30	—
MACS J1311.0-0310	3258	13:11:01.665	-03:10:39.50	14.9	I3	0.4940	5.60	10.00	—
—	6110	—	—	63.2	I3	—	—	—	—
MACS J1621.3+3810	3254	16:21:24.801	+38:10:08.65	9.8	I3	0.4610	7.53	11.50	—
—	3594	—	—	19.7	I3	—	—	—	—
—	6109	—	—	37.5	I3	—	—	—	—
—	6172	—	—	29.8	I3	—	—	—	—
MACS J1931.8-2634	3282	19:31:49.656	-26:34:33.99	13.6	I3	0.3520	6.97	23.40	e
MACS J2049.9-3217	3283	20:49:56.245	-32:16:52.30	23.8	I3	0.3254	6.98	8.71	—
MACS J2211.7-0349	3284	22:11:45.856	-03:49:37.24	17.7	I3	0.2700	11.30	22.20	—
MACS J2214.9-1359	3259	22:14:57.467	-14:00:09.35	19.5	I3	0.5026	8.80	24.10	—
—	5011	—	—	18.5	I3	—	—	—	—
MACS J2228+2036	3285	22:28:33.872	+20:37:18.31	19.9	I3	0.4120	7.86	18.10	—
MACS J2229.7-2755	3286	22:29:45.358	-27:55:38.41	16.4	I3	0.3240	5.01	9.60	—
MACS J2245.0+2637	3287	22:45:04.657	+26:38:03.46	16.9	I3	0.3040	6.06	9.46	—
MKW3S	900	15:21:51.930	+07:42:31.97	57.3	I3	0.0450	2.18	1.14	—
MKW 4	3234	12:04:27.218	+01:53:42.79	30.0	S3	0.0198	2.06	0.03	—
MKW 8	4942	14:40:39.633	+03:28:13.61	23.1	I3	0.0270	3.29	0.85	a,b
MS J0016.9+1609	520	00:18:33.503	+16:26:12.99	67.4	I3	0.5410	8.94	33.20	—
MS J0116.3-0115	4963	01:18:53.944	-01:00:07.54	39.3	S3	0.0452	1.84	-0.00	—
MS J0440.5+0204	4196	04:43:09.952	+02:10:18.70	59.4	S3	0.1900	5.46	2.21	—
MS J0451.6-0305	902	04:54:11.004	-03:00:52.19	44.2	S3	0.5386	8.90	33.60	—
MS J0735.6+7421	4197	07:41:44.245	+74:14:38.23	45.5	S3	0.2160	5.55	7.65	—
MS J0839.8+2938	2224	08:42:55.969	+29:27:26.97	29.8	S3	0.1940	4.68	3.13	—
MS J0906.5+1110	924	09:09:12.753	+10:58:32.00	29.7	I3	0.1630	5.38	4.69	—
MS J1006.0+1202	925	10:08:47.462	+11:47:36.31	29.4	I3	0.2210	5.61	4.81	—
MS J1008.1-1224	926	10:10:32.312	-12:39:56.80	44.2	I3	0.3010	7.45	8.53	—
MS J1455.0+2232	4192	14:57:15.088	+22:20:32.49	91.9	I3	0.2590	4.77	10.40	—
MS J2137.3-2353	4974	21:40:15.178	-23:39:40.71	57.4	S3	0.3130	6.01	11.40	—
MS J1157.3+5531	4964	11:59:52.295	+55:32:05.61	75.1	S3	0.0810	3.28	0.12	b
NGC 507	2882	01:23:39.905	+33:15:21.73	43.6	I3	0.0164	1.40	0.24	c
NGC 4636	3926	12:42:49.856	+02:41:15.86	74.7	I3	0.0031	0.66	-0.00	c
—	4415	—	—	74.4	I3	—	—	—	—
NGC 5044	3225	13:15:23.947	-16:23:07.62	83.1	S3	0.0090	1.22	0.21	c
—	3664	—	—	61.3	S3	—	—	—	—
NGC 5813	5907	15:01:11.260	+01:42:07.23	48.4	S3	0.0066	0.76	0.03	c
NGC 5846	788	15:06:29.289	+01:36:20.13	29.9	S3	0.0057	0.64	0.02	c
Ophiuchus	3200	17:12:27.731	-23:22:06.74	50.5	S3	0.0280	11.12	2.78	—
PKS 0745-191	2427	07:47:31.436	-19:17:39.78	17.9	S3	0.1028	8.50	18.40	—
—	508	—	—	28.0	S3	—	—	—	—
—	6103	—	—	10.3	I3	—	—	—	—
RBS 461	4182	03:41:17.490	+15:23:54.66	23.4	I3	0.0290	2.60	-0.00	a,e
RBS 533	3186	04:19:38.105	+02:24:35.54	10.0	I3	0.0123	1.29	-0.00	—
—	3187	—	—	9.6	I3	—	—	—	—
—	5800	—	—	44.5	S3	—	—	—	—
—	5801	—	—	44.4	S3	—	—	—	—
RBS 797	2202	09:47:12.971	+76:23:13.90	11.7	I3	0.3540	7.68	26.30	d
RX J0220.9-3829	9411	02:20:56.582	-38:28:51.21	19.9	I3	0.2287	4.86	-0.00	—
RX J0232.2-4420	4993	02:32:18.771	-44:20:46.68	23.4	I3	0.2836	7.83	18.30	—
RX J0439+0520	527	04:39:02.218	+05:20:43.11	9.6	I3	0.2080	4.60	3.61	—
RX J0439.0+0715	1449	04:39:00.710	+07:16:07.65	6.3	I3	0.2300	6.50	9.44	—
—	3583	—	—	19.2	I3	—	—	—	—
RX J0528.9-3927	4994	05:28:53.039	-39:28:15.53	22.5	I3	0.2632	7.89	13.10	—
RX J0647.7+7015	3196	06:47:50.029	+70:14:49.66	19.3	I3	0.5840	9.07	26.50	—
—	3584	—	—	20.0	I3	—	—	—	—
RX J0819.6+6336	2199	08:19:26.007	+63:37:26.53	14.9	S3	0.1190	3.87	1.12	—
RX J1000.4+4409	9421	10:00:32.024	+44:08:39.69	18.5	I3	0.1540	3.42	-0.00	—
RX J1022.1+3830	6942	10:22:10.034	+38:31:23.54	41.5	S3	0.0491	3.04	-0.00	f
RX J1130.0+3637	6945	11:30:02.789	+36:38:08.26	49.4	S3	0.0600	2.02	-0.00	—
RX J1320.2+3308	6941	13:20:14.650	+33:08:33.06	38.6	S3	0.0366	1.01	-0.00	e
RX J1347.5-1145	3592	13:47:30.593	-11:45:10.05	57.7	I3	0.4510	10.88	100.00	—
—	507	—	—	10.0	S3	—	—	—	—
RX J1504.1-0248	5793	15:04:07.415	-02:48:15.70	39.2	I3	0.2150	8.00	34.90	—
RX J1532.9+3021	1649	15:32:53.781	+30:20:58.72	9.4	I3	0.3450	5.44	20.80	—
—	1665	—	—	10.0	S3	—	—	—	—
RX J1539.5-8335	8266	15:39:32.485	-83:35:23.83	8.0	I3	0.0728	3.81	-0.00	—
RX J1720.1+2638	4361	17:20:09.941	+26:37:29.11	25.7	I3	0.1640	6.37	11.50	—
RX J1720.2+3536	3280	17:20:16.953	+35:36:23.63	20.8	I3	0.3913	5.65	13.00	—
—	6107	—	—	33.9	I3	—	—	—	—
—	7225	—	—	2.0	I3	—	—	—	—
RX J1852.1+5711	5749	18:52:08.815	+57:11:42.63	29.8	I3	0.1094	3.44	-0.00	—
RX J2129.6+0005	552	21:29:39.944	+00:05:18.83	10.0	I3	0.2350	5.91	12.70	—
SC 1327-312	4165	13:29:47.748	-31:36:23.54	18.4	I3	0.0531	3.53	3.16	f

TABLE 1 — *Continued*

Cluster — (1)	Obs. ID — (2)	R.A. hr:min:sec (3)	Decl. ° : ' : '' (4)	Exposure Time ksec (5)	ACIS — (6)	z — (7)	kT_X keV (8)	$L_{bol.}$ 10^{44} ergs s $^{-1}$ (9)	Notes — (10)
Sersic 159-03	1668	23:13:58.764	-42:43:34.70	9.9	S3	0.0580	2.65	1.10	—
SS2B153	3243	10:50:26.125	-12:50:41.76	29.5	S3	0.0186	0.80	-0.00	—
UGC 3957	8265	07:40:58.335	+55:25:38.30	7.9	I3	0.0341	2.96	-0.00	—
ZWCL 1215	4184	12:17:41.708	+03:39:15.81	12.1	I3	0.0750	6.62	3.52	—
ZWCL 1358+6245	516	13:59:50.526	+62:31:04.57	54.1	S3	0.3280	10.66	12.50	—
ZWCL 1742	8267	17:44:14.515	+32:59:29.68	8.0	I3	0.0757	4.40	-0.00	—
ZWCL 1953	1659	08:50:06.677	+36:04:16.16	24.9	I3	0.3800	7.37	17.30	—
ZWCL 3146	909	10:23:39.735	+04:11:08.05	46.0	I3	0.2900	7.48	29.90	—
ZWCL 7160	543	14:57:15.158	+22:20:33.85	9.9	I3	0.2578	4.53	10.30	—
Zwicky 2701	3195	09:52:49.183	+51:53:05.27	26.9	S3	0.2100	5.21	5.24	—
ZwCl 857.9+2107	7897	09:00:36.835	+20:53:40.36	9.0	I3	0.2350	12.10	-0.00	e

NOTE. — Col. (1) Cluster name; col. (2) CXC CDA Observation Identification Number; col. (3) R.A. of cluster center; col. (4) Decl. of cluster center; col. (5) exposure time; col. (6) observing mode; col. (7) CCD location of cluster center; col. (8) redshift; col. (9) average cluster temperature; col. (10) core entropy measured in this work; col. (11) cluster bolometric luminosity; and col. (12) notes are as follows: (a) - cluster analyzed using the best-fit β -model for the surface brightness profiles (discussed in §3.2); (b) - clusters with complex surface brightness of which only the central regions were used in fitting $K(r)$; (c) - cluster only used during analysis of the *HIFLUGCS* sub-sample (discussed in §5.4); (d) - cluster with central AGN removed during analysis (discussed in §3.5); (e) - cluster with central compact source removed during analysis (discussed in §3.5); and (f) - cluster with central bin ignored during fitting (discussed in §3.5).

TABLE 2
SUMMARY OF β -MODEL FITS

Cluster — (1)	S_{01} 10^{-6} cts/s/arcsec ² (2)	r_{c1} '' (3)	β_1 — (4)	S_{02} 10^{-6} cts/s/arcsec ² (5)	r_{c2} '' (6)	β_2 — (7)	D.O.F. — (8)	χ^2_{red} — (9)
Abell 119	4.93 ± 0.73	39.1 ± 15.3	0.34 ± 0.07	3.52 ± 0.96	735.2 ± 479.4	1.27 ± 1.27	52	1.76
Abell 160	2.32 ± 0.27	53.4 ± 11.1	0.57 ± 0.12	1.29 ± 0.22	284.0 ± 52.2	0.74 ± 0.10	90	1.18
Abell 193	24.72 ± 1.62	80.8 ± 2.2	0.43 ± 0.01	—	—	—	38	0.43
Abell 400	4.66 ± 0.09	151.3 ± 6.4	0.42 ± 0.01	—	—	—	96	0.57
Abell 1060	21.95 ± 0.44	93.5 ± 8.1	0.35 ± 0.01	—	—	—	42	1.44
Abell 1240	1.58 ± 0.07	247.9 ± 46.9	1.01 ± 0.22	—	—	—	58	1.58
Abell 1736	3.81 ± 0.56	55.6 ± 16.1	0.42 ± 0.12	2.49 ± 0.47	1470.0 ± 87.2	5.00 ± 0.73	35	1.58
Abell 2125	3.50 ± 0.20	26.0 ± 4.9	0.49 ± 0.05	1.02 ± 0.13	159.9 ± 9.2	1.32 ± 0.16	35	0.33
Abell 2255	8.38 ± 0.15	222.7 ± 9.8	0.62 ± 0.02	—	—	—	94	1.45
Abell 2256	21.69 ± 0.19	407.8 ± 17.9	0.99 ± 0.05	—	—	—	88	0.83
Abell 2319	47.39 ± 0.61	128.8 ± 3.1	0.49 ± 0.01	—	—	—	92	1.67
Abell 2462	8.19 ± 1.43	60.8 ± 9.6	0.64 ± 0.11	1.87 ± 0.25	762.7 ± 39.1	5.00 ± 0.87	67	1.54
Abell 2631	20.55 ± 1.01	66.0 ± 4.0	0.73 ± 0.03	—	—	—	58	1.15
Abell 3376	4.21 ± 0.09	125.5 ± 5.6	0.40 ± 0.01	—	—	—	98	1.42
Abell 3391	10.65 ± 0.31	132.3 ± 7.9	0.48 ± 0.01	—	—	—	84	1.86
Abell 3395	6.85 ± 0.67	90.9 ± 6.7	0.49 ± 0.03	—	—	—	38	0.96
MKW 8	7.71 ± 0.62	25.2 ± 2.5	0.32 ± 0.01	1.51 ± 0.08	1124.0 ± 64.1	5.00 ± 0.40	88	0.65
RBS 461	12.84 ± 0.34	102.2 ± 4.1	0.52 ± 0.01	—	—	—	84	1.56

NOTE. — Col. (1) Cluster name; col. (2) central surface brightness of first component; col. (3) core radius of first component; col. (4) β parameter of first component; col. (5) central surface brightness of second component; col. (6) core radius of second component; col. (7) β parameter of second component; col. (8) model degrees of freedom; and col. (9) reduced chi-squared statistic for best-fit model.

TABLE 3
M. DONAHUE'S H α OBSERVATIONS.

Cluster —	Telescope —	z —	[NII]/H α —	H α Flux 10^{-15} ergs/s/cm ²
Abell 85	PO	0.0558	2.67	0.581
Abell 119	LC	0.0442	—	<0.036
Abell 133	LC	0.0558	—	0.88
Abell 496	LC	0.0328	2.50	2.90
Abell 1644	LC	0.0471	—	1.00
Abell 1650	LC	0.0843	—	<0.029
Abell 1689	LC	0.1843	—	<0.029
Abell 1736	LC	0.0338	—	<0.026
Abell 2597	PO	0.0854	0.85	29.7
Abell 3112	LC	0.0720	2.22	2.66
Abell 3158	LC	0.0586	—	<0.036
Abell 3266	LC	0.0590	1.62	<0.027
Abell 4059	LC	0.0475	3.60	2.22
Cygnus A	PO	0.0561	1.85	28.4
EXO 0422-086	LC	0.0397	—	<0.031
Hydra A	LC	0.0522	0.85	13.4
PKS 0745-191	LC	0.1028	1.02	10.4

NOTE. — The abbreviation “PO” denotes observations taken on the 5 m Hale Telescope at the Palomar Observatory, USA, while “LC” are observations taken on the DuPont 2.5 m telescope at the Las Campanas Observatory, Chile. Upperlimits for H α fluxes are 3σ .

TABLE 4
STATISTICS OF BEST-FIT PARAMETERS

Sample — (1)	Category — (2)	# Obj — (3)	K_0 keV cm ² (4)	K_{12} keV cm ² (5)	K_{100} keV cm ² (6)	α — (7)
ACCEPT	All	227	72.9 ± 33.7	91.6 ± 35.7	126 ± 44.7	1.21 ± 0.39
HIFLUGCS	—	59	62.3 ± 32.7	87.2 ± 34.5	166 ± 64.9	1.18 ± 0.38
CSE	—	37	61.9 ± 27.4	81.6 ± 31.3	132 ± 45.3	1.19 ± 0.39
β_s	—	17	220 ± 74.1	230 ± 76.9	67.4 ± 27.0	1.45 ± 0.47
ACCEPT	$4 < K_0 < 50$ keV cm ²	98	17.5 ± 5.84	31.2 ± 10.3	148 ± 49.3	1.21 ± 0.39
HIFLUGCS	—	25	13.6 ± 4.61	29.4 ± 9.63	174 ± 57.3	1.15 ± 0.37
CSE	—	0	—	—	—	—
ACCEPT	$K_0 \leq 50$ keV cm ²	105	16.1 ± 5.70	30.5 ± 10.0	150 ± 49.9	1.20 ± 0.38
HIFLUGCS	—	29	11.4 ± 4.21	31.2 ± 10.5	235 ± 89.3	1.17 ± 0.37
CSE	—	19	15.6 ± 5.22	30.9 ± 10.2	146 ± 47.9	1.16 ± 0.38
ACCEPT	$K_0 > 50$ keV cm ²	122	156 ± 53.6	175 ± 58.6	107 ± 39.2	1.23 ± 0.40
HIFLUGCS	—	30	151 ± 52.5	172 ± 58.3	113 ± 42.9	1.19 ± 0.39
CSE	—	18	148 ± 48.9	165 ± 53.7	118 ± 42.1	1.23 ± 0.40

TABLE 4 — *Continued*

Sample	Category	# Obj	K_0	K_{12}	K_{100}	α
—	—	—	keV cm ²	keV cm ²	keV cm ²	—
(1)	(2)	(3)	(4)	(5)	(6)	(7)

NOTE. — Listed here are the mean best-fit parameters of the model $K(r) = K_0 + K_{100}(r/100 \text{ kpc})^\alpha$ for various sub-groups of the full *ACCEPT* sample. The 'CSE' sample are the clusters with a central source excluded (discussed in §3.5). The K_{12} values represent the entropy at 12 kpc and are calculated from the best-fit models. Col. (1) Sample being considered; col. (2) the sub-group of the sample; col. (3) number of objects in the sub-group; col. (4) mean best-fit K_0 ; col. (5) mean entropy at 12 kpc; col. (6) mean best-fit K_{100} ; and col. (7) mean best-fit power-law index.

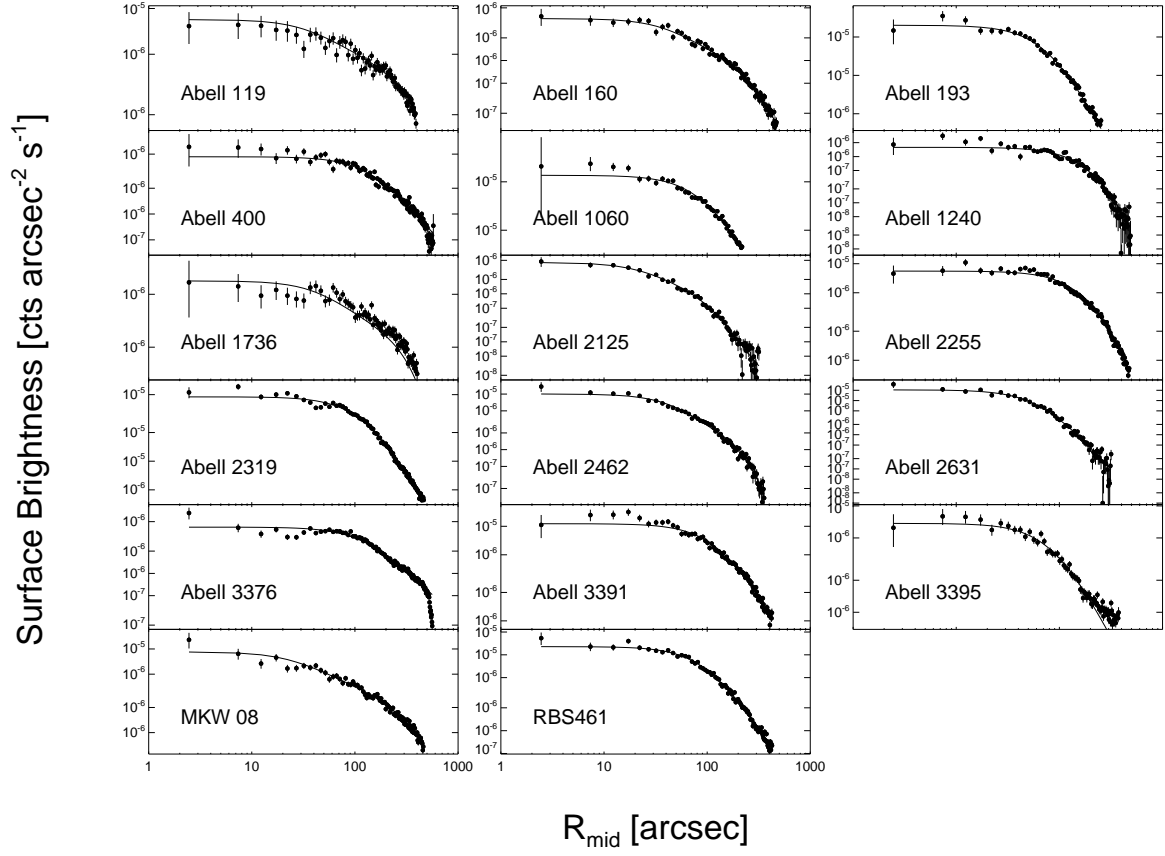


FIG. 1.— Surface brightness profiles for clusters requiring a β -model fit (discussed in §3.3). The best-fit β -model for each cluster is overplotted as a dashed line. The discrepancy between the data and best-fit model for some clusters results from the presence of a compact X-ray source at the center of the cluster. These cases are discussed in Appendix A.

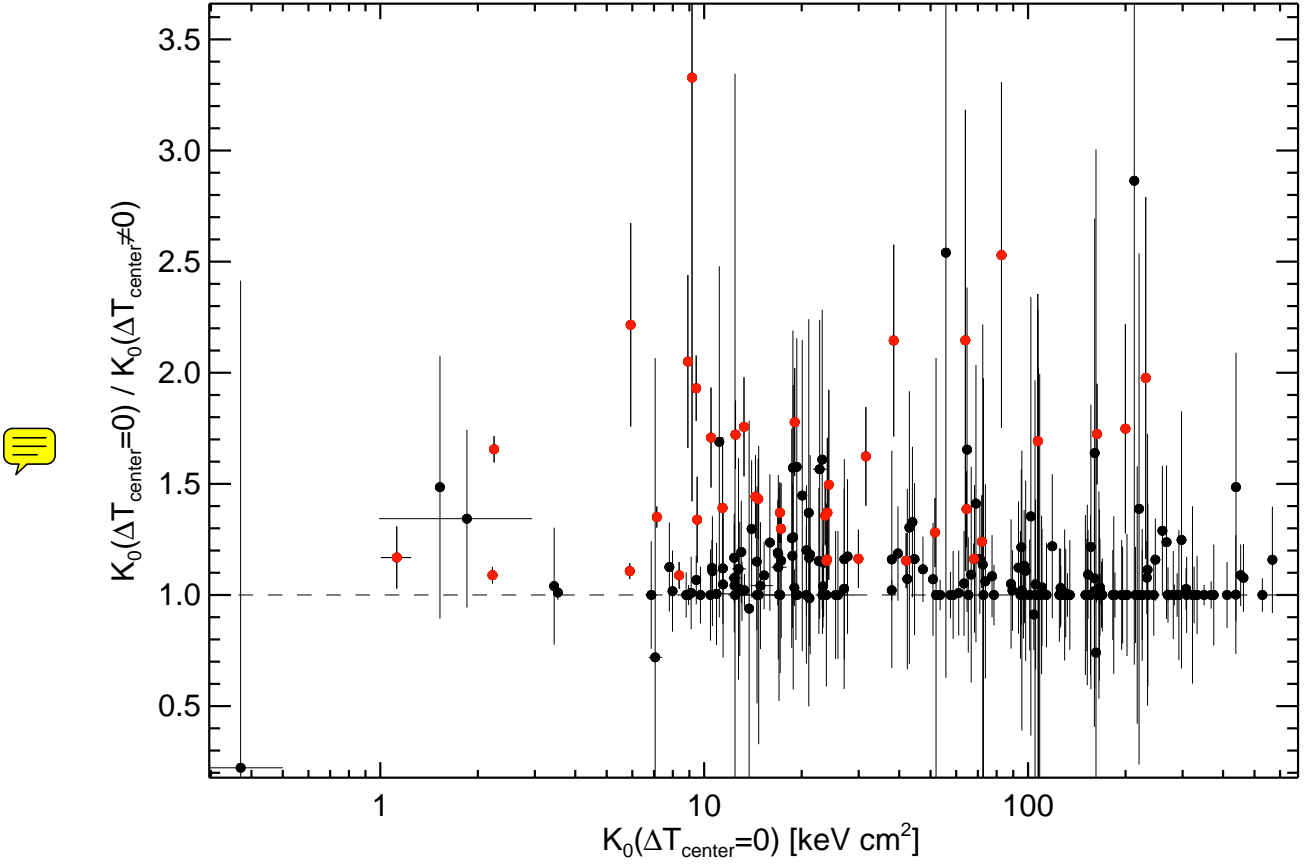


FIG. 2.— Ratio of best-fit K_0 for the two treatments of central temperature interpolation (see §3.1): (1) temperature is free to decline across the central density bins ($\Delta T_{\text{center}} \neq 0$), and (2) the temperature across the central density bins is isothermal ($\Delta T_{\text{center}} = 0$). Red points are clusters for which the K_0 ratio is inconsistent with unity, however, all of these clusters have steep temperature gradients which result in unsubstantiated cool temperatures in their cores when kT_X is extrapolated to small radii.

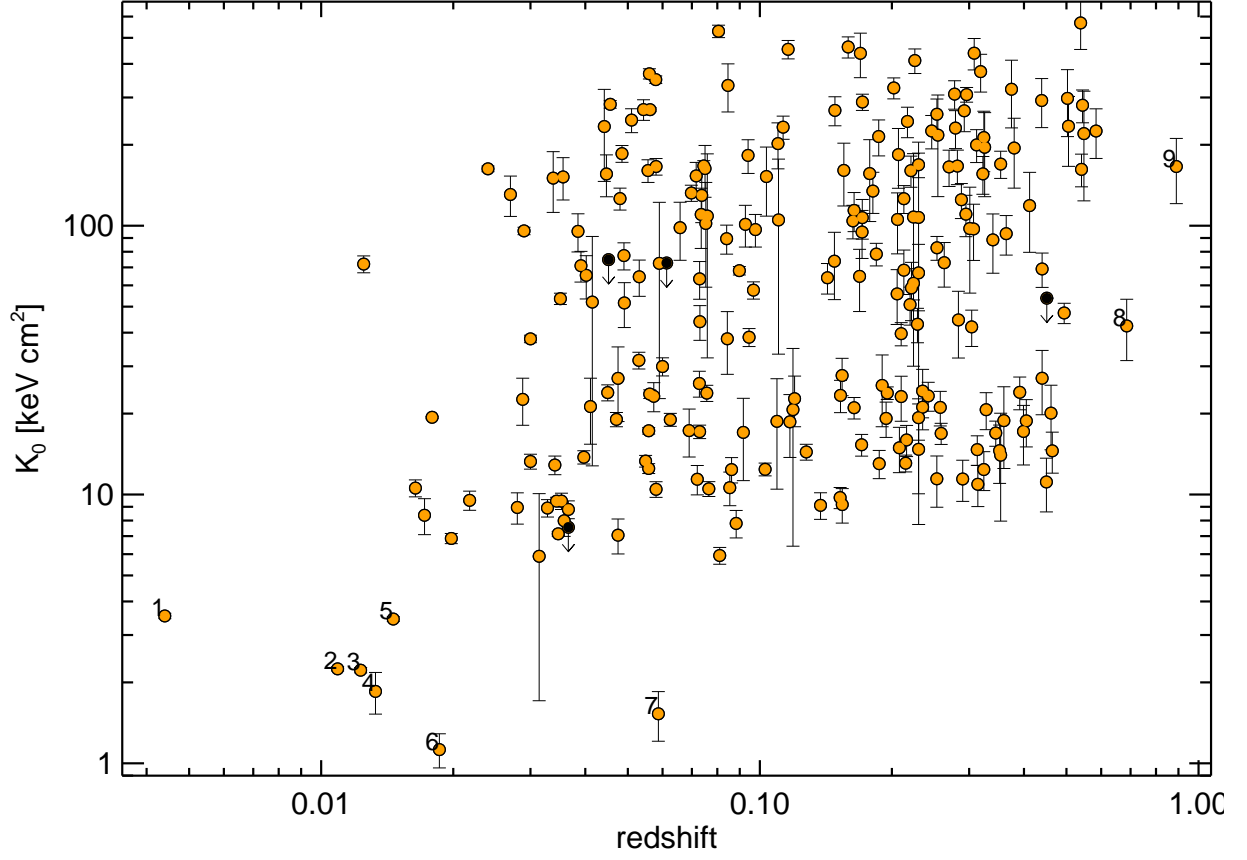


FIG. 3.— Best-fit K_0 vs. redshift. Some clusters have K_0 error bars smaller than the point. The clusters with upper-limits (black points with downward arrows) are: A2151, AS0405, MS 0116.3-0115, and RX J1347.5-1145. The numerically labeled clusters are: (1) M87, (2) Centaurus Cluster, (3) RBS 533, (4) HCG 42, (5) HCG 62, (6) SS2B153, (7) A1991, (8) MACS0744.8+3927, and (9) CL J1226.9+3332. For CLJ1226, Maughan et al. (2007) found best-fit $K_0 = 132 \pm 24 \text{ keV cm}^2$ which is not significantly different from our value of $K_0 = 166 \pm 45 \text{ keV cm}^2$. The lack of $K_0 < 10 \text{ keV cm}^2$ clusters at $z > 0.1$ is most likely the result of insufficient angular resolution (see §4.2).

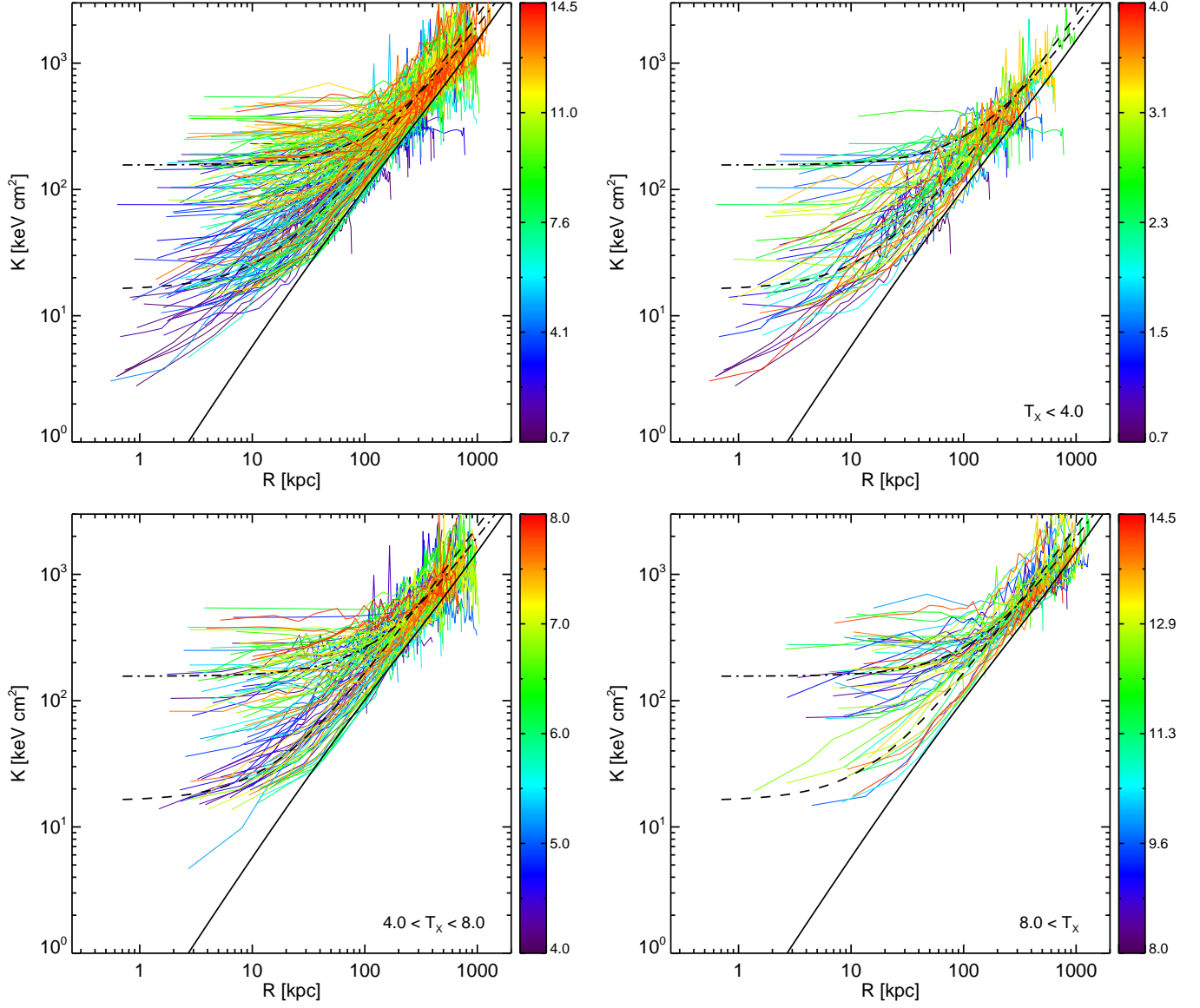


FIG. 4.— Composite plots of entropy profiles for varying cluster temperature ranges. Profiles are color-coded based on average cluster temperature. Units of the color bars are keV. The solid-line is the pure-cooling model of Voit et al. (2002), the dashed-line is the mean profile for clusters with $K_0 \leq 50$ keV cm², and the dashed-dotted line is the mean profile for clusters with $K_0 > 50$ keV cm². *Top left:* This panel contains all the entropy profiles in our study. *Top right:* Clusters with $kT_x < 4$ keV. *Bottom left:* Clusters with $4 \text{ keV} < kT_x < 8 \text{ keV}$. *Bottom right:* Clusters with $kT_x > 8$ keV. Note that while the dispersion of core entropy for each temperature range is large, as the kT_x range increases so to does the mean core entropy.

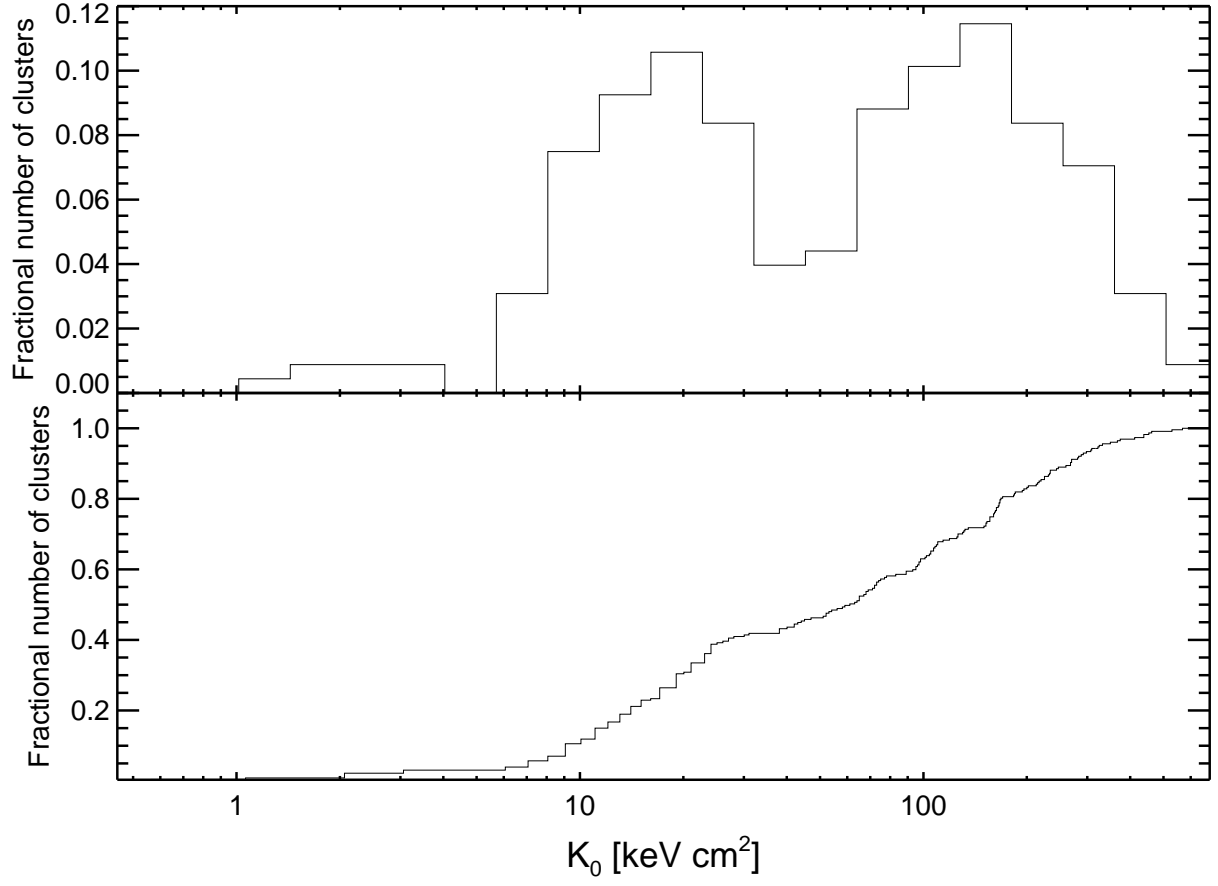


FIG. 5.— *Top panel:* Histogram of best-fit K_0 for all the clusters in *ACCEPT*. Bin widths are 0.15 in log space. *Bottom panel:* Cumulative distribution of K_0 values for the full sample. The distinct bimodality in K_0 is present in both distributions, which would not be seen if it were an artifact of the histogram binning. A KMM test finds the K_0 distribution cannot arise from a simple unimodal Gaussian.

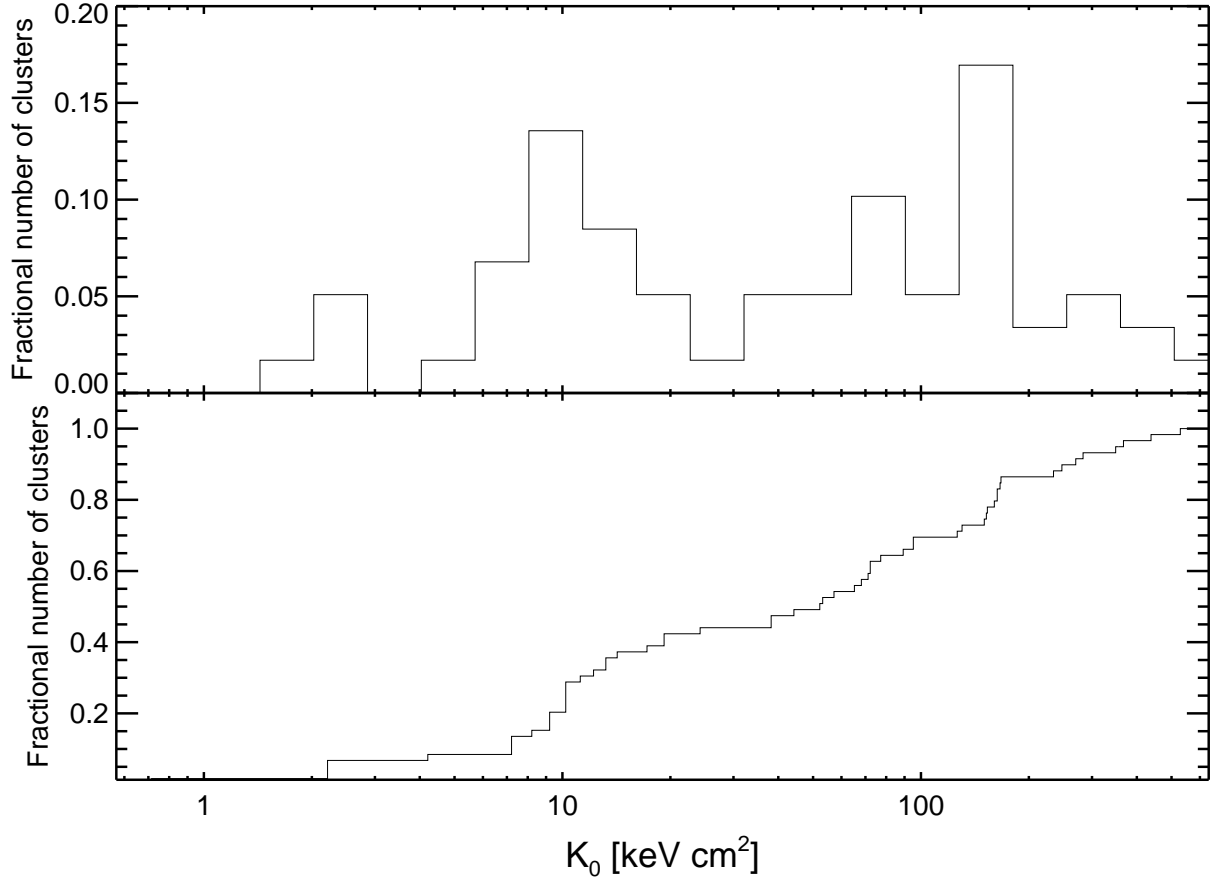


FIG. 6.— *Top panel:* Histogram of best-fit K_0 values for the primary *HIFLUGCS* sample. Bin widths are 0.15 in log space. *Bottom panel:* Cumulative distribution of best-fit K_0 values. The distinct bimodality seen in the full *ACCEPT* sample (Fig. 5) is also present in the *HIFLUGCS* subsample and shares the same gap ~~starting at $K_0 \approx 30 \text{ keV cm}^2$~~ . That bimodality is present in both samples is strong evidence it is not a result of an unknown archival bias.

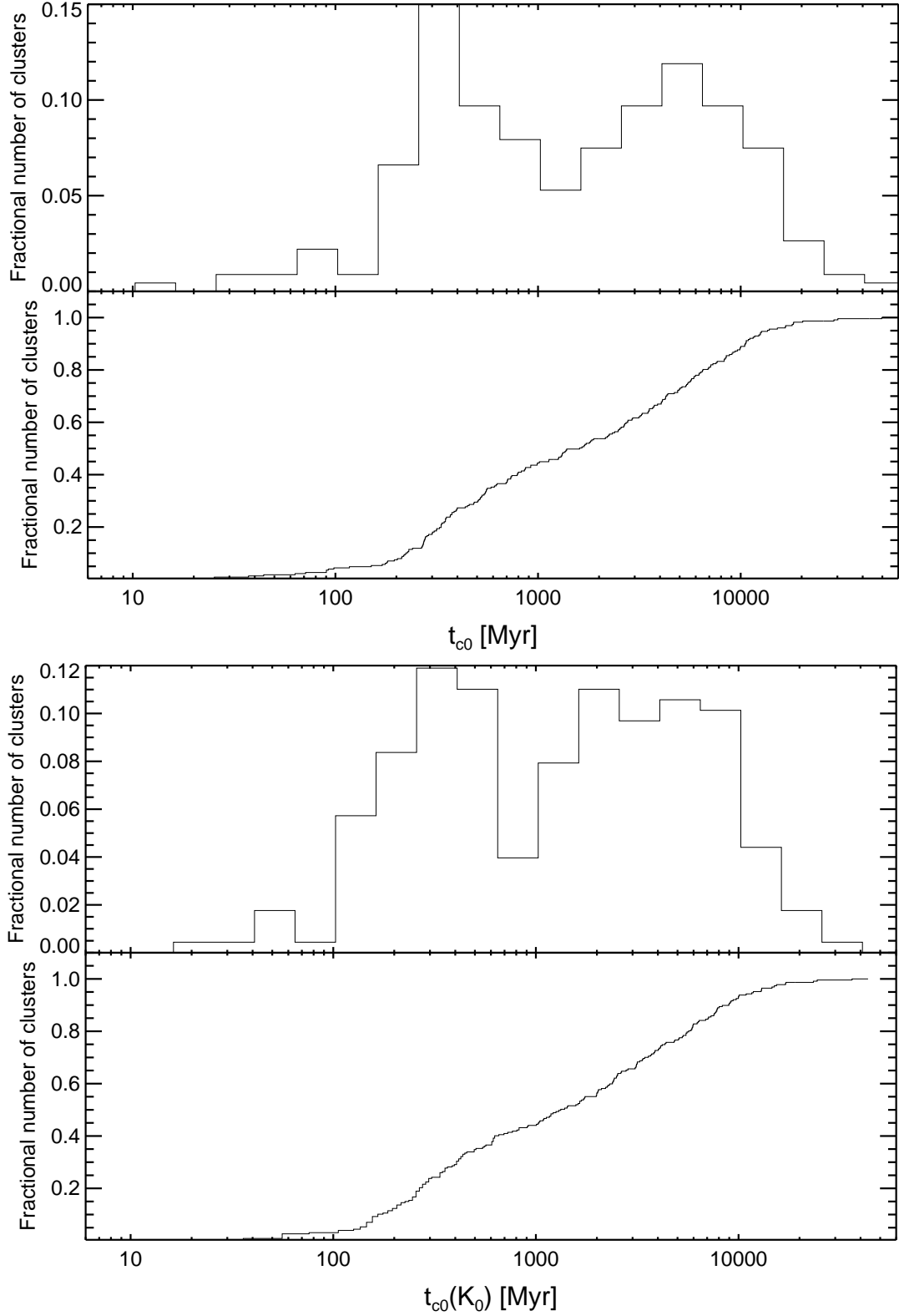


FIG. 7.— *Top panel:* Log-binned histogram and cumulative distribution of best-fit core cooling times, t_{c0} (eqn. 8), for all the clusters in *ACCEPT*. Histogram bin widths are 0.2 in log space. *Bottom panel:* Log-binned histogram and cumulative distribution of core cooling times calculated from best-fit K_0 values, $t_{c0}(K_0)$ (eqn. 9), for all the clusters in *ACCEPT*. Histogram bin widths are 0.2 in log space. The bimodality we observe in the K_0 distribution is also present in best-fit t_{c0} . However, the gaps between the two populations of t_{c0} and $t_{c0}(K_0)$ differ by ~ 0.3 Gyrs with scaled-entropy having the more pronounced gap with a shorter cooling time.

